remote sensing

MDPI

Article

High-Precision 3D Object Capturing with Static and Kinematic Terrestrial Laser Scanning in Industrial Applications—Approaches of Quality Assessment

Ulrich Stenz [1], Jens Hartmann [2,*], Jens-André Paffenholz [3] and Ingo Neumann [2]

[1] Geo-Office Gesellschaft für graphische Datenverarbeitung und Vermessung mbH, Karl-Liebknecht-Straße 101, 14612 Falkensee, Germany; ulrich.stenz@geo-office.de

[2] Geodetic Institute, Leibniz Universität Hannover, Nienburger Str. 1, 30167 Hannover, Germany; neumann@gih.uni-hannover.de

[3] Institute of Geotechnical Engineering and Mine Surveying, Department Mine Surveying and Geoinformation, Clausthal University of Technology, Erzstraße 18, 38678 Clausthal-Zellerfeld, Germany; jens-andre.paffenholz@tu-clausthal.de

* Correspondence: hartmann@gih.uni-hannover.de; Tel.: +49-511-762-4469

Received: 1 November 2019; Accepted: 8 January 2020; Published: 15 January 2020

Abstract: Terrestrial laser scanning is used in many disciplines of engineering. Examples include mobile mapping, architecture surveying, archaeology, as well as monitoring and surveillance measurements. For most of the mentioned applications, 3D object capturing in an accuracy range of several millimeters up to a few centimeters is sufficient. However, in engineering geodesy, particularly in industrial surveying or monitoring measurements, accuracies in a range of a few millimeters are required. Additional increased quality requirements apply to these applications. This paper focuses on the quality investigation of data captured with static and kinematic terrestrial laser scanning. For this purpose, suitable sensors, which are typically used in the approach of a multi-sensor-system, as well as the corresponding data capturing/acquisition strategies, are presented. The aim of such systems is a geometry- and surface-based analysis in an industrial environment with an accuracy of +/− 1–2 mm or better.

Keywords: high-precision terrestrial laser scanning; multi-sensor-systems; kinematic laser scanning; laser tracker; forward modeling; backward modeling; quality analysis; industrial surveying; calibration; synchronization

1. Introduction

Terrestrial laser scanning (TLS) is used in many disciplines of engineering. Examples include mobile mapping, architecture surveying, archaeology, as well as monitoring and surveillance measurements. For most of the mentioned applications, 3D object capturing in an accuracy range of several millimeters up to a few centimeters is sufficient. However, in engineering geodesy, particularly in industrial surveying or monitoring measurements, accuracies in a range of a few millimeters are required. Additional increased quality requirements apply to these applications.

This paper focuses on the quality investigation of data captured with static (s-TLS) and kinematic laser scanning (k-TLS). For this purpose, suitable sensors and multi-sensor-systems (MSS), as well as the capturing methods, are presented. The aim of such systems is a geometry- and surface-based analysis in an industrial environment with an accuracy of +/−1–2 mm or better.

The precision and accuracy of 3D point cloud capturing depends on various influencing factors, which makes the evaluation of 3D point clouds obtained with TLS a complex task. The uncertainty budget of 3D point clouds consists of, e.g.,

- external influences or atmospheric conditions (temperature, air pressure, etc.) [1];
- properties of the captured object (color, material, shape) [2,3];
- sensor-internal influences (axis error, tumbling error, linearity deviation) [4–6];
- measurement set-up (distance, angle of incidence horizontal and vertical) [1,7,8];
- (geo-) referencing including stationing and registration (referencing means framing in a local and geo-referencing in a global reference frame, (geo-) referencing implies that both is possible).

Compared to s-TLS, k-TLS-based MSS (k-TLS as an object-capturing sensor, combined with additional sensors for (geo-) referencing the laser scanner on a moving platform) use a different method of (geo-) referencing (determine the trajectory of the k-TLS-based MSS) [9]. Here, additional sensors, which will inevitably increase the uncertainty budget, are used. A distinction is made between internal and external (geo-) referencing. For internal (geo-) referencing, additional sensors, for example, GNSS, inertial measuring units (IMU), odometer or camera systems, are used. The external (geo-) referencing is based on classical measuring systems such as total stations. Current system developments do not have the specifications to meet all these requirements and conditions. Examples for indoor applications in the industry are the Leica ProScan [10], Trimble Indoor Mobile Mapping Solution (TIMMS) [11], iMS2D/iMS3D [12] and indoor applications from science and research [13]. For outdoor purposes, exemplary applications from science are shown in [14,15] and for the industry, KiSS and MoSES [16] and the Leica ProScan [1]. From this, it can be deduced that different/suitable k-TLS-based MSS must be used. The main difference can be found in the (geo-) referencing method, which must be done with significantly higher accuracy.

For the k-TLS-based MSS presented in this paper, external (geo-) referencing is performed by a laser tracker (LT). Here, a Leica Absolute Tracker 960 Long Range (AT960 LR) in combination with a Leica T-Probe is used. This setting makes it possible to record a total of six degrees of freedom (DoF), consisting of three translations and rotations. The combination of multiple sensors to an MSS requires a system calibration for the MSS and the synchronization of the individual sensors in addition to the previously mentioned individual sensor calibration. The additional factors influencing the total uncertainty budget for k-TLS are as follows:

- stationing of the sensor used for the external (geo-) referencing in the reference frame;
- external (geo-) referencing of the moving platform;
- synchronization of the individual MSS sensors;
- system calibration (calibration of the sensing sensor to the referencing sensors).

To determine the precision and accuracy of the k-TLS-based MSS, the literature provides various approaches, which can be subdivided into the so-called forward and backward modeling. The forward modeling approaches are based on the intensity values of the laser scanner measurements [17,18] and on Monte Carlo simulations which are used to derive a synthetic variance–covariance matrix [2]. Backward modeling approaches are mainly 3D point clouds to point cloud comparisons (Cloud2Cloud) [19]. Surface based approaches are shown in [20,21]. The comparison of captured 3D point clouds to highly accurate 3D reference point clouds [22] is suitable here to investigate the accuracy.

Section 2 addresses the construction and function of the k-TLS-based MSS with highly accurate (geo-) referencing developed at the GIH. To evaluate the quality of the data from s- and k-TLS, two evaluation approaches, forward and backward modeling, are presented in Section 3 (a detailed description of the experimental set-up, sensors and infrastructure used in this approach can be found in [22]). Here, the focus is on the variation of the measurement geometries for s-TLS. The goal is to show the effects of the above influencing factors (in particular, distance and angle of incidence) on the measurements (Section 4). K-TLS-based MSSs have the possibility to adapt the distance and horizontal angle of incidence to the captured object (Section 4). A comparison of s-TLS to k-TLS should show whether these possibilities of k-TLS-based MSS lead to an improvement of the accuracy in the acquisition of 3D point clouds accuracy. It will also be investigated whether these benefits are

compensated for by the additional factors (system calibration, synchronization, and (geo-) referencing of the mobile platform) that influence the accuracy (Section 5).

Under laboratory conditions, the suitability of the presented system to reach the high-precision requirements of industrial surveying is shown [22]. The following article will show the transferability of the system to real conditions within an industrial environment.

2. 3D Object Capturing with TLS and TLS-Based MSS

TLS is mostly used to be able to perform rapid and areal 3D object capturing. In industrial surveying, very strict accuracy requirements apply to the 3D measuring process. In recent years, s-TLS has been established as a standard procedure capable of meeting these requirements, see [22,23]. For long, stretched objects (e.g., ships, aircrafts, wind power turbines), several standpoints are needed in the classic s-TLS approach. The 3D point clouds from each standpoint must be subsequently transferred to a common coordinate system. With an increasing number of standpoints, this can be very time consuming and inefficient. In these cases, object capturing with k-TLS is recommended. In addition to better efficiency, this allows for a constant optimization of the angle of incidence between the laser beam and the object's surface. The disadvantage is that additional sensors must be used, which increase the costs of the system and the overall uncertainty budget. For the k-TLS-based MSS described here, additional limitations arise due to the working range of the LT—maximum measurement distance of 20 m and the maximum rotation (pitch and yaw angle) of the T-probe of 45° [24]. As already mentioned, k-TLS-based MSS use additional sensors for (geo-) referencing besides the laser scanner as the object-capturing sensor. The following sections provide a brief overview of the sensors used for s-TLS at the Geodetic Institute Hannover (GIH) and the developed MSS for k-TLS with their basic measuring principles.

2.1. Relevat Sensors for as the s- and k-TLS-Based MSS at the GIH

Within this study, we use the laser scanners shown in Figure 1 (Z + F Imager 5006 (Figure 1a), and Imager 5016 (Figure 1b) as well as the Imager 5010X), which are used for s- and k-TLS. The k-TLS-based MSS (Figure 1f) is tracked by the LT Leica AT960 LR (Figure 1c) in conjunction with the Leica T-Probe (Figure 1e) as referencing sensors. The triangulation-based hand-held scanner Leica T-Scan 5 (Figure 1d) was used in combination with the AT960LR at GIH for high-accurate acquisition of the reference data [22].

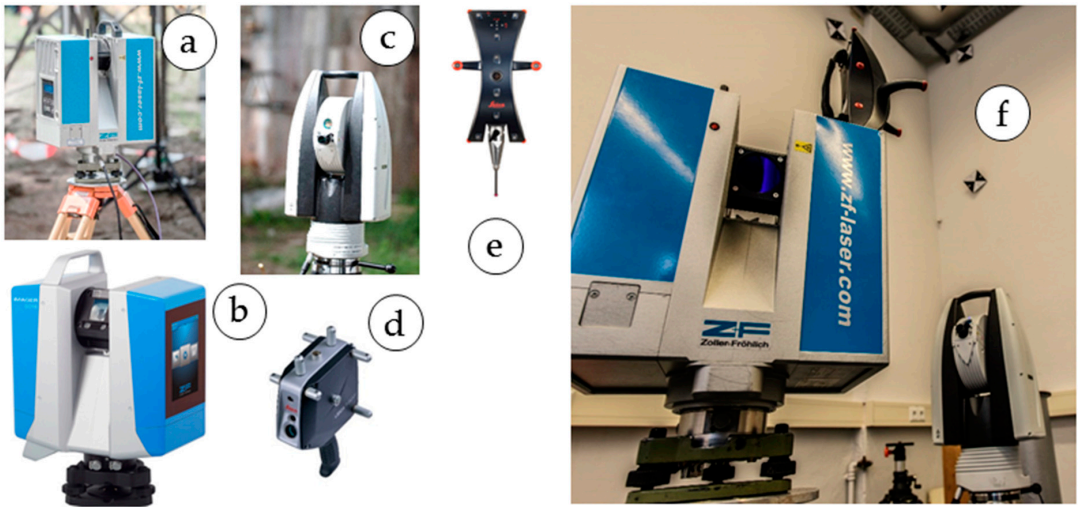

Figure 1. Sensors used at the Geodetic Institute Hannover (GIH) (**a**) Z + F Imager 5010X; (**b**) Z + F Imager 5016 (zf-laser.com), (**c**) Leica AT960 LR; (**d**) Leica T-Scan 5 (metrology.leica-geosystems.com); (**e**) Leica T-Probe (www.hexagonmi.com); (**f**) k-terrestrial laser scanning (TLS)-based multi-sensor-systems (MSS) consisting of laser scanner Z + F Imager 5006, Leica T-Probe, Leica AT960 LR [22].

2.2. Measuring Principles of s-TLS

The measuring principle of s-TLS is well described in the common literature, e.g., [25,26]; therefore, a detailed description is not given here. More complex or larger objects usually require several standpoints for an entire capturing. The 3D point clouds of the individual standpoints must be referenced or (geo-) referenced in order to transform all 3D point clouds into a common coordinate system with an optional known geodetic datum. This can be done by stationing points, which can be natural or artificial, and must be present in adjacent 3D point clouds. Artificial points can be ensured by different kinds of targets. As an example, spheres or targets with a checkerboard pattern can be mentioned here. An exemplary configuration with several stand points is shown in Figure 2.

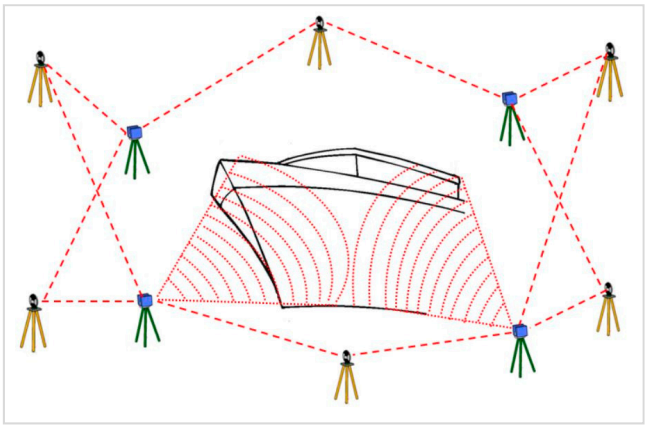

Figure 2. Principles of object capturing with s-TLS (green) using identical points as signalized targets (yellow).

Furthermore, the individual 3D point clouds must be registered (aligned) to each other. To register the 3D point clouds, various approaches are described in the literature. Here, for example, an automatic registration based on planes [27], registration with the Iterative Closest Point ICP Algorithm [28] or surface based algorithms [29] are possible. The registration can also be done manually via the described natural or artificial stationing points. For registration via artificial points, checkerboard targets (Figure 3) are used at the GIH. These targets can be measured by laser scanners and LT, and they enable a photogrammetric analysis [22].

(**a**) (**b**)

Figure 3. Target mount for the combined adaption of the targets and corner cube reflectors (CCRs) (**a**) target front, target mount with CCR, target back; (**b**) CCR, target mount with target, target back [22].

A more efficient process in object capturing and in the registration process can be obtained by k-TLS-based MSS.

2.3. Measuring Principles of the k-TLS-Based MSS

The principle of object capturing with a k-TLS-based MSS is shown in Figure 4. Here, a laser scanner, operating in 2D-profiler mode and mounted on a kinematic platform, is moved along the object of interest [30,31].

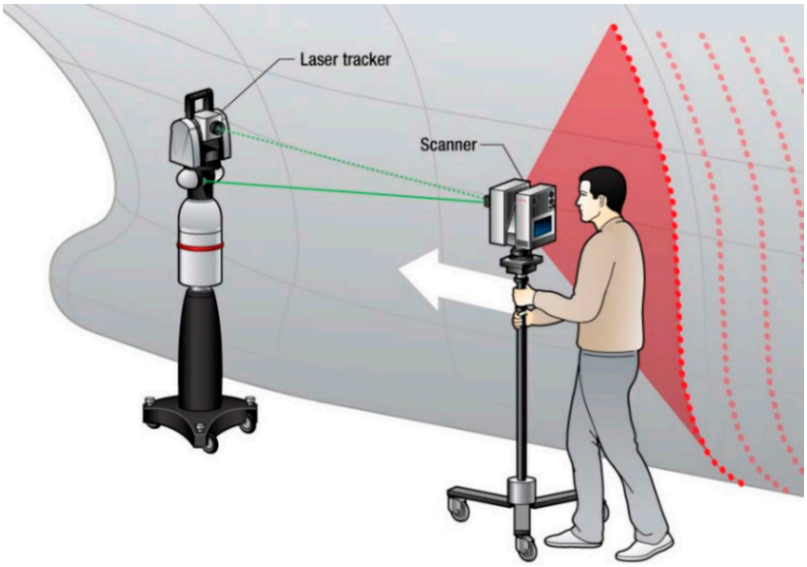

Figure 4. Functional principle of the k-TLS-based MSS during object capturing [30].

The object-capturing-related sensor is a TLS with high accuracy. Among the uncertainty factors listed in Section 1, a 3D total uncertainty of < ±1 mm maximum permissible error (MPE) is expected within a measurement distance of <10 m. In order to obtain such highly accurate results, a Leica AT960 LR is used in conjunction with a laser-scanner-mounted Leica T-Probe (Figure 5) for the highly accurate direct (geo-) referencing of the moving platform. The direct (geo-) referencing by laser tracker measurements was first presented by Dr. Hesse und Partner Ingenieure (DHPI) in 2012 [30]. The LT is equipped with an absolute interferometer (AIFM). The advantage is that the distance measurement is carried out with the accuracy of an absolute distance meter and with the speed of an interferometer. That means, a distance measurement with up to 1000 points per second and an accuracy of ±0.5 µm/m [24] can be performed even without a reference point. Fast and accurate measurements are possible in this way even without a reference point. Furthermore, the laser tracker has a camera (Leica T-Cam), through which the reference points on the T-Probe, consisting of 10 light-emitting diodes are measured (Figure 5).

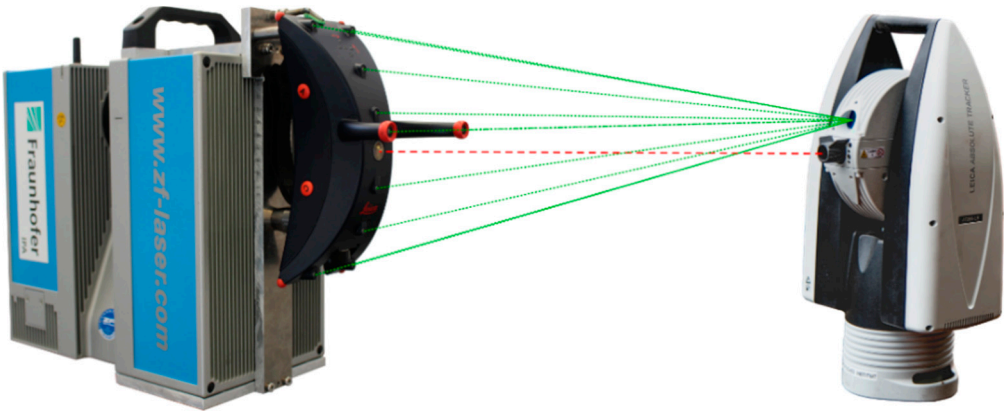

Figure 5. Measuring of the reference points mounted on T-Probe with the Leica AT960 LR (10 measured LEDs in green, measured distance to reflector in red).

This makes it possible to determine three translations and three rotations (6 DoF) simultaneously. Therefore, the position of the T-Probe is determined directly. By using a trigger signal, which the laser scanner (per profile) sends to the LT, a synchronization of the 3D object acquisition and the (geo-) referencing is performed and a continuous tracking of the kinematic platform is ensured. Due to the fact that a 2D profile consists of a defined number of points, only the first point of a profile is thus accurately (geo-) referenced. In order to ensure a pointwise (geo-) referencing for all points of the 2D profile, the movement of the platform between the detected individual poses must be considered. In a Kalman filter, a point-precise (geo-) referencing of all profile points can be performed. The position, velocity and acceleration are estimated within the filter. Therefore, the prediction steps allow for the calculation for each point. Figure 6 shows the geometric structure of such a scanned TLS profile.

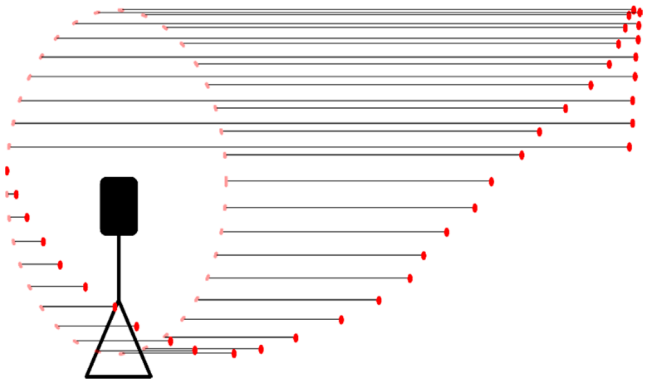

Figure 6. Point by point (geo-) referencing of a k-TLS.

Even with a dynamic platform movement, it is, therefore, ensured that the (geo-) referencing takes place pointwise and with high accuracy. In [31] a k-TLS measurement of a mockup was (geo-) referenced accordingly and compared to s-TLS with the multiple model to model cloud comparison M3C2 algorithm described in [32]. The standard deviation of the calculated distances between the k-TLS and s-TLS is 1 mm.

Since the coordinate system of the T-Probe (CTP) is three-dimensionally shifted and rotated, relative to the coordinate system of the laser scanner (CLS), the relative pose must be determined. This process is referred to as 6 DoF system calibration [33]. An overview of the sensors used, and their coordinate systems is shown in Figure 7. The highly accurate determination of the 6 DoF is based on a common acquisition of reference geometries by LT and laser scanners and is fundamentally described in [30]. The determination of the translations is carried out with a standard deviation of a few tenths of a millimeter and the rotations with a few milli degrees. Investigations are described in [34–36]. Thus, all measured points can be transformed by the CLS into the CLT. The transformation of the points into the CLT corresponds to a similarity transformation with seven parameters, whereby the scale is typically set to 1.0. The transformation from CLS to CLT involves a two-step strategy as follows:

- First transformation step: transformation from CLS to CTP with the 6 DoF of the previous calibration;
- Second transformation step: from the CTP to the CLT with the translations and rotations directly measured by the LT to the T-Probe.

The suitability for the introduced k-TLS-based MSS and classical s-TLS for the application in the industrial environment shall be discussed in the following sections. Furthermore, we will show that a quality assurance for the k-TLS-based MSS can be obtained. This quality assurance process can be carried out in a forward and backward manner.

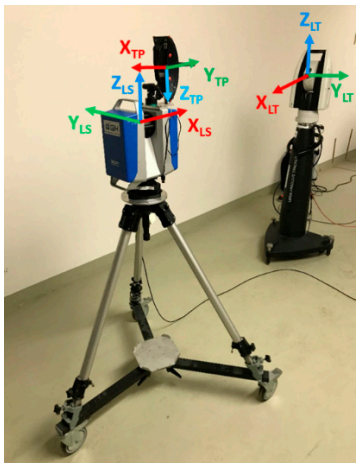

Figure 7. Overview of the sensors used for the k-TLS-based MSS with their coordinate systems. The 6 DoF are assumed to be constant for the measurement period. The results from test measurements on reference geometries measured with a Leica T-Scan show that the 3D object capturing by k-TLS with a standard deviation of 1–2 mm is possible [22,31,34] (distance to object approximately 5–10 m).

3. Quality Evaluation Approaches—Forward and Backward Modeling

Based on these two evaluation approaches, the data of the presented TLS-based MSS/systems will then be examined in various test and application scenarios.

For both approaches, a suitable infrastructure must be provided, which allows highly accurate data acquisition in a high-accurate reference frame. Both approaches require a suitable reference point field for (geo-) referencing and registration of the 3D point clouds. The backward modeling additionally requires suitable reference geometries for laboratory investigations. When measuring in an industrial environment, reference geometries must be identified on the object to be measured in order to enable realistic measurement situations.

3.1. Highly Accurate Reference Frame for s- and k-TLS in Forward and Backward Modeling Approaches

An essential contribution to the accuracy of the measurement results, especially for the registration and the (geo-) referencing of the individual 3D point clouds, is the provision of a highly accurate reference network. Here are several factors to consider:

- Realization of the reference system via the reference points and their signalization;
- Measurement of the reference network with high accuracy (at least one order of magnitude better than the required accuracy of the object acquisition of the tested system).

In the realization of the reference system and its signalization, the following factors must be taken into account:

- A sufficient number of well-distributed reference points;
- Use of targets which enable the highly accurate determination of the reference points (manufacturing and, if necessary, calibration of the targets, highly accurate detection of the targets center).

Within this frame of reference, various work steps must be carried out which have an influence on the achievable accuracies in object capturing. These are in particular:

- Measuring and adjustment of the reference network;
- Stationing the LT (k-TLS) or the laser scanner (s-TLS) within the reference network;
- (Geo-) referencing of the object-capturing TLS (s- and k-TLS);
- System and sensor calibration of k-TLS;

- Synchronization at k-TLS.

A short overview concerning the infrastructure needed and used for investigations can be found in Section 4. A comprehensive implementation can be found in [22].

3.2. Forward Modeling—Quality Analysis of 3D Point Clouds Derived from s- and k-TLS-Based MSS Derived from Intensity Values

In addition to angle and distance measurements, most TLS also observe intensity values for each captured point. The intensity of the reflected laser beam in TLSs is of great importance for the precision of the distance measurement. The author of [17] shows in his approach how to derive precision information from the intensity values. Based on the assumption that the noise of the distance measurement depends on the energy of the received signal [37], intensity measurements must be considered regarding precision as a quality parameter. In addition to the inversely proportional decrease of the intensity values to the square of the distance, the angle of incidence and material properties also have an influence on the measurement uncertainty. Therefore, the laser scanners used must undergo a calibration process to estimate the laser-scanner-specific calibration parameters of the stochastic model. This calibration process for a specific laser scanner contains different steps. In addition to the calibration set-up shown in [17] with varying distances (Figure 8), the influence of the angle of incidence is investigated (Figure 9). The goal of the calibration process is to estimate the calibration parameters a and b of the stochastic model (1) [17] for the used TLS.

$$\sigma_{dist} = a \times I^b, \tag{1}$$

where I = intensity value and σ_{dist} = standard deviation of the distance measurement.

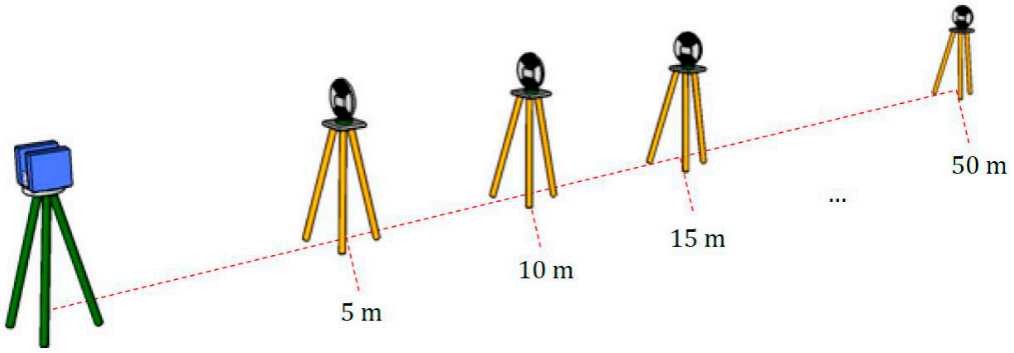

Figure 8. Calibration set-up investigating distance- and target-dependent reflectivity with varying target grey values [38].

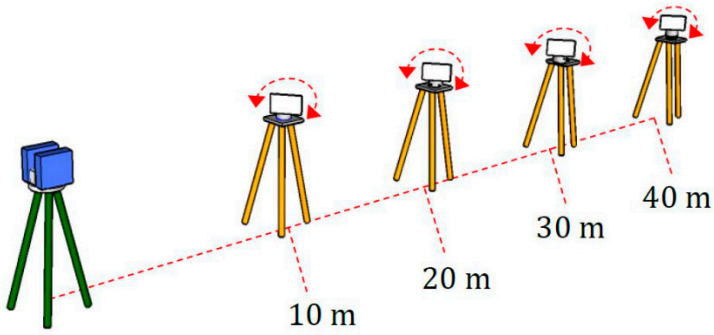

Figure 9. Calibration set-up investigating distance and angle of incidence [38].

Laboratory measurements must be performed to estimate the calibration parameters. Therefore, eight targets with differing grey values (0% black–100% black) were measured at different distances (5

to 50 m, Figure 8) using the one-dimensional measurement mode (the horizontal and vertical motor are disabled) of the TLS. Single points are measured here with high frequency for thirty seconds.

In a second step, the influence of the angle of incidence was investigated. A target was placed on a micrometer rotation table and the angle of the target towards the TLS was varied in steps of 10° (from −80° to +80°). A one-dimensional measurement was carried out in each position as already mentioned previously (Figure 9).

To implement this approach, a laser scanner is required which can be operated in 1D mode and which delivers the intensity values. This is the case for some large manufacturers (Z + F, Leica, Wetzlar, Germany). For laser scanners from brands that do not offer these possibilities, other approaches [20,21] can be chosen. The precision determined with this approach includes the influences of the distance measurement, the angle of incidence and the object properties. Internal sensor effects, such as axis deviations, are not taken into account. For laser scanners with manufacturer calibration, however, these effects are negligible or can be determined separately.

3.2.1. Estimation of Calibration Parameters

Following the stochastic model shown in [17,38], the calibration measurements were performed, the parameters a and b (1) were calculated for the TLS used (Zoller + Fröhlich Imager 5006 and Imager 5010X). Based on the results, the functional model was extended. In addition to the calibration parameters a and b, an offset c (2) was introduced. This offset was estimated using a target with high reflectivity (5 m distance, 0% black), leading to the new stochastic model (2).

$$\sigma_{dist} = a \times I^b + c, \tag{2}$$

Three conclusions can be drawn from the experiments for both scanners:

- The noise of the distance measurement increases with increasing distance.
- Low reflectivity leads to higher noise, where lower intensity appears at high distances and flat angles of incidence.
- Flat angles of incidence lead to less precision in the distance measurements (under 1 mm at a 30° angle of incidence, 4 mm at 10° angle of incidence for highly reflecting targets and under 3 mm at 40° for low-reflecting targets).

Detailed information about, e.g., complete settings of the experiments carried out by the used laser scanners and the developed program with graphical user interface for different sensors and settings) can be found in [38]. Furthermore, the authors of [38] present graphical and numerical results for varying distances and angles of incidence, as well as a comparison to the results described in [17]. All the influences shown are subsumed in the intensity-based approach. The model does not cover other systematic influences, such as an axis or a tumbling deviation.

3.2.2. Stochastic Information for 3D Coordinates

A propagation of the standard deviation of the polar elements (3), according to the law of variance propagation, makes it possible to transfer the stochastic information to 3D coordinates (4).

$$\sum_{dist,\theta,\lambda} = \begin{bmatrix} \sigma_{dist}^2 & 0 & 0 \\ 0 & \sigma_\theta^2 & 0 \\ 0 & 0 & \sigma_\lambda^2 \end{bmatrix} \begin{bmatrix} \left(a * I^b + c\right)^2 [m]2 & 0 & 0 \\ 0 & (0.007)^2 [^\circ]2 & 0 \\ 0 & 0 & (0.007)^2 [^\circ]2 \end{bmatrix}, \tag{3}$$

With σ_θ = standard deviation of vertical angle, according to the manufacturer's datasheet and σ_λ = standard deviation of horizontal angle, both according to the manufacturer's datasheet.

$$\sum_{X,Y,Z} = A * \sum_{dist,\theta,\lambda} * A^T, \tag{4}$$

With X, Y, Z = Cartesian 3D coordinates and d, θ, λ = distance, vertical angle, horizontal angle. The matrix A includes the partial derivations of the Cartesian 3D coordinates.

For this, the assumption is made that:

- the standard deviation of the angle measuring device is considered as a constant for all measurements in the calculation and
- that there are no correlations between the polar elements.

As a representative quality parameter, Helmert's point error $\sigma_{x,y,z}$ (5) is derived for each 3D point via the diagonal elements of the variance–covariance matrix (4).

$$\sigma_{x,y,z} = \sqrt{\sigma_x^2 + \sigma_y^2 + \sigma_{\theta_z}^2}, \tag{5}$$

3.3. Backward Modeling Based on Reference Data with High Accuracy

Backward modeling based on reference data with high accuracy requires an infrastructure described in detail in [22].

Within this infrastructure, reference data is collected with high accuracy. These data must be captured with a sensor that achieves an accuracy of one order of magnitude better than the required accuracy of ±1 mm (i.e., 0.1 mm and better). Backward modeling investigates the following:

- the differences between the reference data and the data collected with TLS by comparing, e.g., geometric parameters derived from reference geometries or
- the direct point cloud to point cloud distances, calculated with the M3C2.

This evaluation element is implemented in both the s- and k-TLS data analyses. The following section provides a brief overview of the infrastructure used at the GIH. A complete overview is provided in [22].

4. Framework and Data Sampling for the Quality Assessment

In the first section, the framework and its acquisition with a higher accuracy are described. In the second section, the accuracy-influencing factors of s- and k-TLS are described in detail.

4.1. Infrastructure for Quality Assessment Based on Reference Data with High Accuracy

The reference data mentioned above are acquired by means of the Leica T-Scan5 (T-Scan) in conjunction with the Leica AT960 LR (Figure 1c,d). This sensor combination delivers the accuracies presented in Table 1.

Table 1. Accuracy of sensors used for providing the reference data [24,39].

Sensor	Accuracy
Leica AT960 LR	$U_{x,y,z}$ = ±15 µm + 6 µm/m (3D accuracy, MPE)
Leica T-Scan 5	$U_{x,y,z}$ = ±60 µm under 8.5 m (MPE)
	U_P = ±80 µm + 3 µm/m (2 σ, uncertainty for plane surfaces, which is defined as the value of all deviations from the best-fit plane that is calculated with all measured points)

Using these sensors, different reference geometries (Figure 10, right) were captured in the GIH 3D laboratory (Figure 10, left). In an industrial environment, the mock-up (Figure 11) was captured with the same sensor set-up.

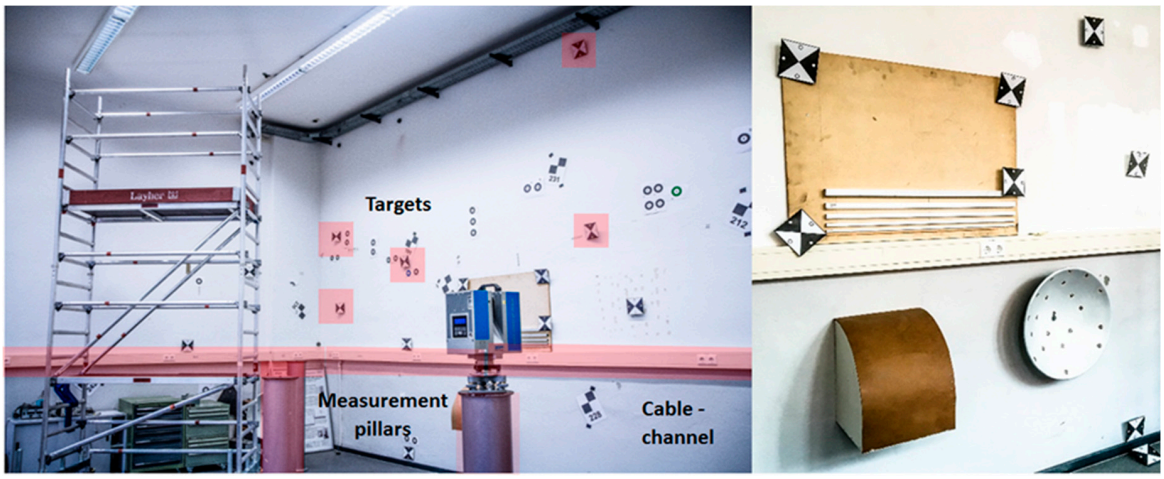

Figure 10. The 3D-laboratory of the GIH with measurement pillars and cable channel (**left**) and reference geometries (**right**) [22].

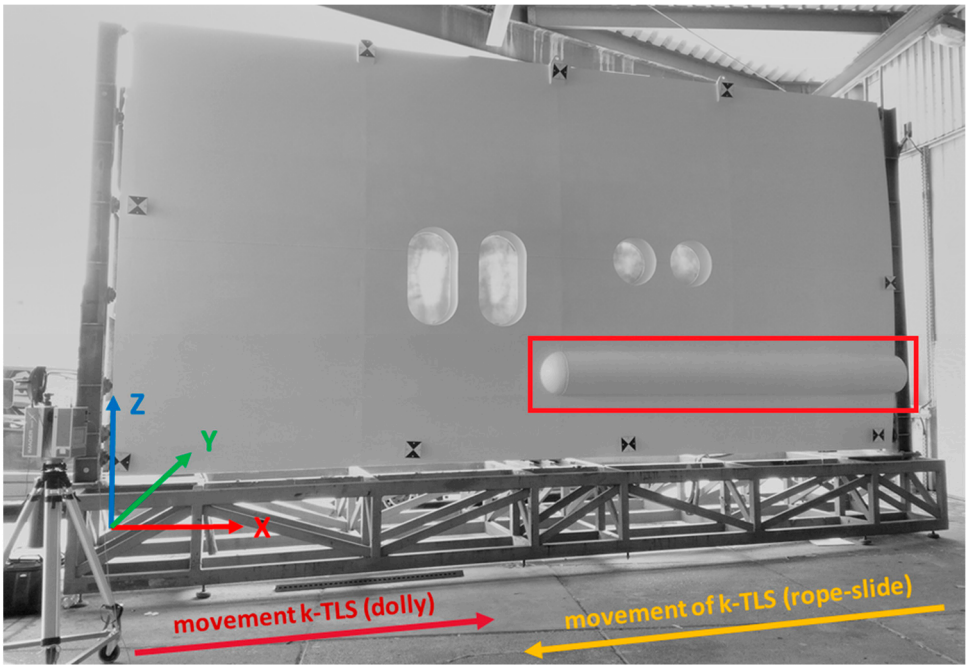

Figure 11. Mock-up with reference points signalized by checkerboard targets (Figure 3), origin of the reference frame. Moving direction of k-TLS and investigated (Section 5) cylindrical geometry marked with red frame.

Within the measurement in the laboratory, as well in the industrial environment, a unique coordinate system was realized by reference points. The measurements were performed with the laser tracker to CCRs and they are described in detail in Section 4.2.1. The signalization of the reference points was carried out by means of the targets shown in Figure 3. The measured 3D point clouds to be compared with the reference 3D point cloud are based on the s- and k-TLS Systems. Here, the Z + F Imager 5006 (3D laboratory) and the Z + F Imager 5010X (industrial environment) were used. In the k-TLS mapping of the objects, a mobile platform based on a dolly (Figures 7 and 12) and a rope-slide (Figure 13) were used. The design of the mobile platforms was kept simple here. It should be noted that neither damping elements nor a gimbal were used in the performed measurements.

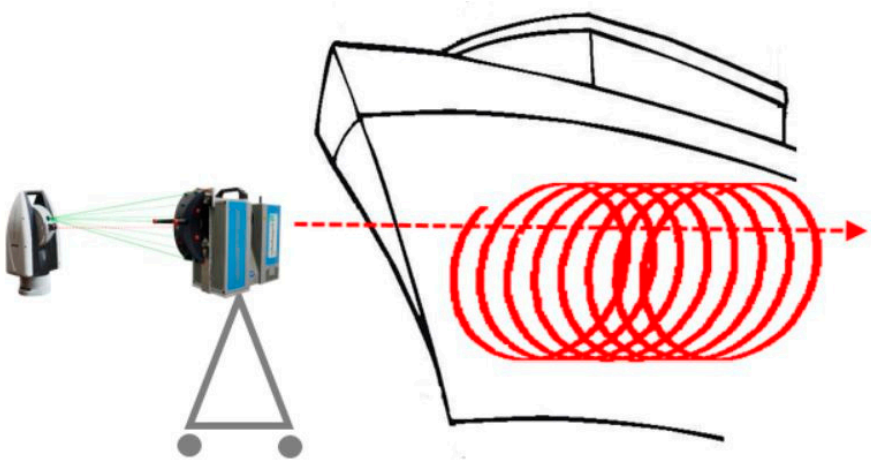

Figure 12. Platform for k-TLS consisting of Z + F Imager 5010X working in 2D profiler mode, mounted on a dolly, (geo-) referenced by Leica AT960 and Leica T-Probe. The moving direction is marked by the red arrow. Movement and profiler mode are resulting in the shown scan helix.

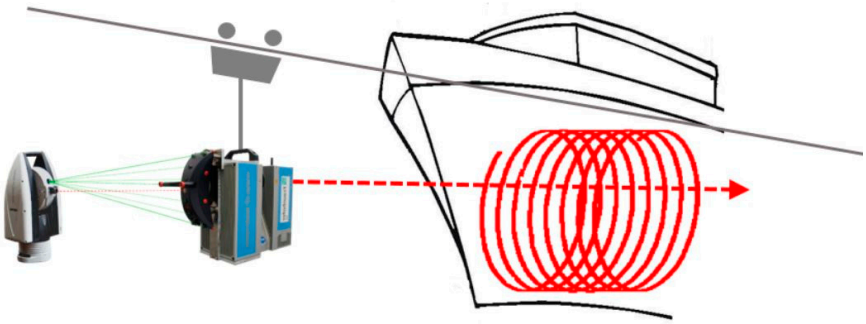

Figure 13. Platform for k-TLS consisting of a Z + F Imager 5010X working in profiler mode, mounted on a rope-slide, (geo-) referenced by Leica AT960 and Leica T-Probe. The moving direction is marked by the red arrow. Movement and profiler mode are resulting in the shown scan helix.

4.2. Specification of the Accuracy-Influencing Factors

As mentioned in Section 1, other factors in addition to the 3D object acquisition, must be taken into account for a determination of the total uncertainty budget of s- and k-TLS. The sub-steps mentioned in Section 1 need to be specified in more detail. In the consideration presented here, the individual sub-steps are considered to be independent, since their determination is carried out separately.

4.2.1. Determination of the Reference Frame (s- and k-TLS)

Before the 3D object measurement, the determination of the reference network takes place. This reference system is used for stationing and (geo-) referencing of the LT and the laser scanner. The reference framework is realized by reference points which are installed in sufficient numbers and well distributed around the object to be measured. For the physical realization of the reference points, the combination of magnetic target mounts and Red Ring CCRs shown in Figure 3 are used. The measurements are done with the LT, with the accuracies shown in Table 1. Subsequently, the coordinates of the reference points are determined, introducing all measurements in a common adjustment. This is done using the Unified Spatial Metrology Network (USMN) of Spatial Analyzer® (SA, New River Kinematics, Williamsburg, WV, USA). By a least-squares fitting, the coordinates are determined on the basis of the measured values and their accuracy measures. Different degrees of accuracy measures and weighting for the individual measuring elements can be introduced [40].

The measurements to the 56 reference points at the 3D laboratory [Figure 14] of the GIH were carried out from three different LT stations. Afterwards, the adjustment was processed with SA. The

standard deviation as a parameter for the accuracy of the reference points after adjustment amounts to 0.05 mm. A detailed description of the reference frame and the process of its determination is shown in [22]. In case of the mock-up, nine reference points from two LT stations were measured. Here, all reference points were determined with a standard deviation of $\sigma_{ref} < 0.1$ mm.

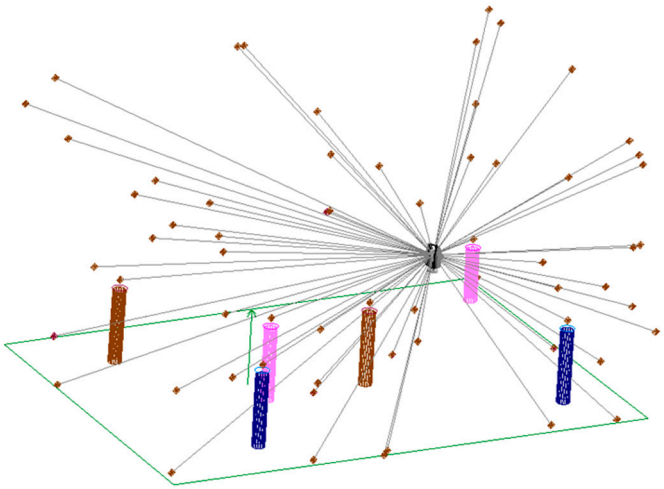

Figure 14. Measurement and adjustment of the 56 reference points at the 3D-measurement laboratory of the GIH [22].

4.2.2. Stationing of the Laser Tracker (k-TLS)

In the stationing process of the LT, measurements to the reference points are carried out. At least four, spatially well distributed reference points should be measured. Afterwards, the transformation parameters between the local coordinate frame of the LT and the superordinate reference frame are determined by a best-fit. The difference between the current pose of the LT and the ending pose is referred to as the transformation. For the mock-up measurements, all nine reference points were measured by the LT and a standard deviation was achieved.

4.2.3. Stationing of the TLS and (geo-) Referencing of the Mobile Platform

Within the reference frame, the position of the laser scanner in the static set-up (s-TLS) and on the mobile platform (k-TLS) is determined. For s-TLS, the stationing of the laser scanner is done by the artificial reference points.

For the stationing of the laser scanner within the reference frame of the mock-up, a standard deviation of 0.3 mm was reached (according to protocol of the used software for the stationing, Z + F LaserControl, Zoller and Fröhlich GmbH, Wangen, Baden-Wurttemberg, Germany) and a maximum distance to the targets of 10 m.

As described in Section 2.3, the (geo-) referencing of the k-TLS-based MSS is carried out by a 6 DoF measurement of the LT to the T-Probe. According to the manufacturer, the uncertainty values are given as MPE, whereby realistic values are more likely to be half of the given MPE [24]. Within the scope of static 6 DoF (geo-) referencing test measurements, the standard deviations of all parameters were determined. In the case of the translations, a similar order of magnitude as the half-MPE values was achieved. For the rotations, a standard deviation of 0.001°–0.002° were obtained.

Due to the fact that systematic deviations are difficult to detect with the used measurement set-up, the half-MPE values for the translations and the obtained standard deviations for the rotations are considered here. Table 2 shows the MPE of the measured parameters and the corresponding standard deviations. The used uncertainties are considered according to GUM (guide to the expression of uncertainty in measurement) [41].

Table 2. Accuracy and standard deviations [24].

Parameter	Maximum Permissible Error (MPE)	Used Standard Deviation σ
translations	$u_{t_x\ t_y\ t_z} = 15\ \mu m + 6\frac{\mu m}{m}$	$\sigma_{t_x\ t_y\ t_z} = 7.5\ \mu m + 3\frac{\mu m}{m}$
rotations	$u_{roll,pitch,yaw} = 0.01^\circ = 18\ \frac{\mu m}{m}$	$\sigma_{roll,pitch,yaw} = 0.002^\circ = 4\ \frac{\mu m}{m}$

The standard deviation of the translations consists of a constant part of 7.5 µm and distance-dependent part of 3 µm/m. The impact of the standard deviation of the three rotations is dependent on the distance. This is achieved by:

$$\mathbf{t}_{xyz}^{rot} = \mathbf{t}_{xyz} \cdot \mathbf{R}_{xyz}, \tag{6}$$

where $\mathbf{t}_{xyz}$ represents the vector of the measured translations $(t_x,\ t_y,\ t_z)$. The rotation matrix $\mathbf{R}_{xyz} = \mathbf{R}_x(\sigma_{roll}) \cdot \mathbf{R}_y\left(\sigma_{pitch}\right) \cdot \mathbf{R}_z\left(\sigma_{yaw}\right)$ consists of the three rotation matrices filled with their corresponding respective standard deviations $\sigma_{roll,pitch,yaw}$ in the three coordinate directions. Detailed information about the structure of the rotation matrices is given by the authors of [25]. The vector $\mathbf{t}_{xyz}^{rot}$ is the rotated vector of the measured translations. The difference of vector $\mathbf{t}_{xyz}^{rot}$ and $\mathbf{t}_{xyz}$ can be interpreted as a 3D deviation, whereby the three elements are summarized with (5). This results in a combined standard deviation of all rotations σ_{rot}. The standard deviation for the (geo-) referencing measurement is achieved by

$$\sigma_{(geo-)\ ref.} = \sqrt{\sigma_{t_x\ t_y\ t_z}^2 + \sigma_{rot}^2}. \tag{7}$$

Strictly speaking, this consideration is only valid for the time of the (geo-) referencing measurement, i.e., to the first point in the profile. For the 3D standard deviation of all further profile points, the predicted displacement from the filter step, which is explained in Section 2.3, must also be taken into account. This should be considered in the future by means of a variance–covariance propagation. Here, the determined standard deviations of the estimated parameters from the filter step are used.

4.2.4. System Calibration for k-TLS

The procedure of the system calibration, where the 6 DoF between the origin of the laser scanner and the T-Probe are determined, was explained in Section 2.3. Within this, the three translations $(t_x,\ t_y,\ t_z)$ can be determined with a standard deviation of $\sigma_{t_x\ t_y\ t_z} \leq 0.1$ mm and the three rotations $(roll, pitch, yaw)$ with $\sigma_{roll,pitch,yaw} \leq 0.001^\circ - 0.002^\circ$ [36]. The standard deviations of the three translations are independent of the distance to the object. This results in a 3D standard deviation σ_{xyz}, which is obtained with (5). The impact of the standard deviations of the rotations instead depends on the distance. The combined standard deviation σ_{rot} is obtained in a similar procedure to the (geo-) referencing with (6) and (5), see Section 4.2.3. The combined standard deviation of the translations and rotations $\sigma_{syst.calib.}$ is calculated with (7).

4.2.5. Synchronization for k-TLS

For synchronization purposes, a trigger that initiates a related measurement is the most precise method and, therefore, it is used for strictly simultaneous actions. For this reason, an exact assignment of the captured profiles and (geo-) referencing measurements is realized. Only a very slight delay is due to appear with:

- the electronic generation of the trigger signal (laser scanner);
- the cable-based signal transmission (not exact vertical rising flanks in the trigger pulse), so that a certain time passes until the required threshold value is reached and
- the receiver electronics at the LT.

The order of magnitude of the delay time in the cable depends on the conductive material, and according to the authors of [42], it is typically 5 ns per meter of cable. According to the authors of [43],

the delay caused by electronic circuits in signal generation and signal reception ranges from a few nanoseconds to over 100 ns. According to the authors of [44], the steepness of the edge of the signal results in delays of about 0.5 µs. Thus, in the worst case, a total delay of 0.75 µs occurs for a 30 m-long cable, which was used in these measurements. In Table 3, the uncertainties with a total delay of 0.75 µs and with respect to the mean velocities of the used platforms are shown.

Table 3. Uncertainties resulting of a total delay of 0.75 µs with respect to the mean velocities of the used platforms.

Platform	Mean Velocity [m/s]	Uncertainty [µm]
dolly	0.127	10
rope-slide	0.685	51

Thus, the influence due to signal delays is negligible here.

5. Application of the Back- and Forward-Modeling

For data analysis, geometric parameters of specific geometric elements in the different data sets are computed and compared. A backward modeling is performed for the assessment of the point cloud accuracy. Therefore, the captured point clouds of the s- and k-TLS are compared with the T-Scan data set by the M3C2 algorithm [32]. In addition, a forward modeling is performed. As described in Section 3.2, the 3D standard deviations of each point are calculated based on the recorded intensities of the s- and k-TLS data. In case of the k-TLS, the uncertainties, which are specified in Section 4.2, are considered.

5.1. Measurements in the 3D Laboratory (s-TLS, k-TLS and T-Scan)

As described in Section 4.1, laboratory measurements are carried out to perform a back- and forward-modeling-based quality analysis for s- and k-TLS. Thus, a whole process for data analysis based on reference data with superordinate accuracy was defined and documented according to [22]. Therefore, various measurements with T-Scan, s- and k-TLS (Figure 15) have been accomplished.

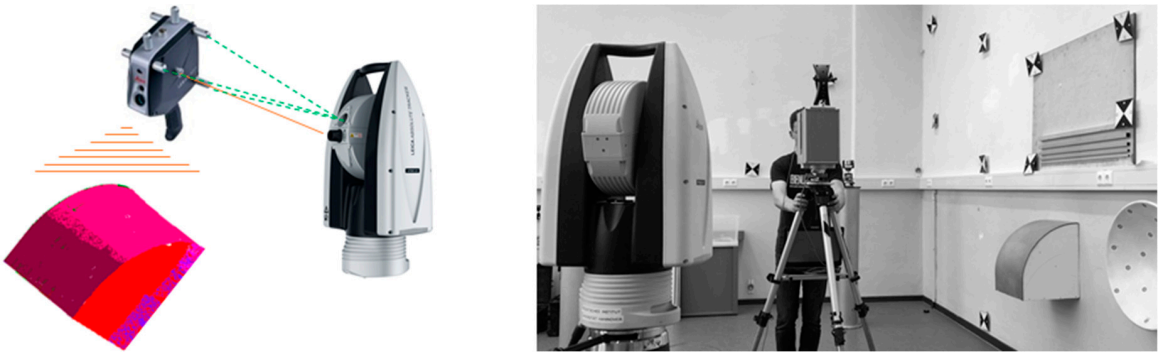

(**a**) (**b**)

Figure 15. Measurement of the reference geometries at the 3D laboratory of the GIH using T-Scan and laser tracker (**a**) and k-TLS with laser scanner, laser tracker and T-Probe (**b**) [22].

The following sections intended to show that a transfer of the laboratory approach according to [22] into a real industrial environment is possible.

5.2. Measurements at the Industrial Environment (s-TLS, k-TLS and T-Scan)

As described in Section 4.1, the object acquisition of the mock-up (Figure 11) was performed by T-Scan, as well as s- and k-TLS measurements. In order to compare the data to each other, a unique

reference frame was implemented. The determination of the reference frame was carried out as described in Section 4.2.1 by high-accuracy LT measurements. The coordinates were determined using the Unified Spatial Metrology Network (USMN) in SA. In the stationing of the LT, the deviations, resulting from the adjustment, amount to < ±0.1 mm.

Within this reference frame, the laser scanner was stationed at three different standpoints (left, middle and right) within 4 m in front of the mock-up, performing static scans. The measurement parameters for the s-TLS are shown in Table 4.

Table 4. Parameters for s-TLS measurements at the industrial environment from (datasheet Z + F IMAGER 5010).

Laser Scanner	Resolution	Quality
Z + F IMAGER 5010C	high 10,000 Pixel/360 deg	normal 25 rps/273 kHz

A high resolution means that the laser scanner captures 10,000 points in the vertical as well as in the horizontal direction. Normal quality means that the laser scanner measures with a frequency of 273 kHz and rotates with 25 rps (rounds per second). Subsequently, the data were transformed into the reference frame via all nine reference points using Z + F LaserControl®. This results in an average 3D point deviation of ±0.6 mm and a standard deviation of the deviations of ±0.3 mm for the stationing.

For the 3D object capturing with the k-TLS-based MSS, the two described platforms from Section 4.1 were used. Table 5 shows the measurement parameters for the laser scanner. For one scenario, a mobile dolly (Figure 12) was used. This was moved at an angle of 45° along the object at a slow pace and for a distance of ~4 to 6 m. In the second scenario, the measurements were performed by an inclined rope-slide (Figure 13). Due to the force of gravity, the acceleration of the cable carriage was achieved. The maximum speed of the platform was 1 m/s and the measuring distance was about ~3 to 5 m.

Table 5. Parameters of the k-TLS measurements with dolly and slip-line.

Platform	Frequency [Hz]	Number of Profiles	Points per Profile
dolly	50	2791	20,000
rope-slide	50	1028	20,000

The main direction of movement was in the direction of the *x*-axis of the reference frame (Figure 11).

As a result of the T-Scan measurements, a highly accurate 3D point cloud of the mock-up, and 3D point clouds of the s- and k-TLS, were achieved. Based on this data, the forward and backward modeling for the quality assurance are performed.

5.3. Data Analysis

Based on the collected 3D point clouds, three different kinds of data analysis were carried out. In the backward modeling approach, geometric parameters derived from 3D point clouds captured by s- and k-TLS and geometric parameters derived from the T-Scan measurements were obtained (Section 5.3.1). Furthermore, a direct comparison of the complete 3D point clouds (TLS compared to T-Scan), using the M3C2 algorithm, was performed (Section 5.3.2). The third evaluation is the forward modeling approach by using the intensity-based model (Section 5.3.3).

5.3.1. Backward Modeling-Based on Geometric Parameters

The following evaluation approach is based on the cylindrical part of the mock-up (Figure 11 marked with a red rectangle). In a first step, a cylinder is estimated from the 3D point cloud acquired with the T-Scan (Figure 16).

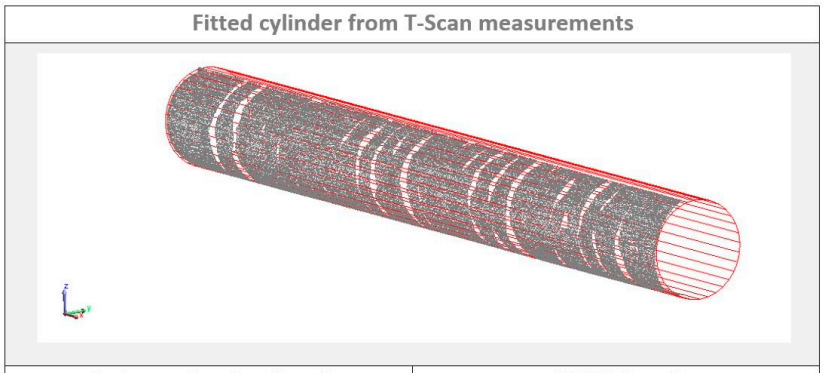

Estimated radius [mm]	RMSE [mm]
215.426	1.286

Figure 16. Estimated cylinder from the 3D point cloud acquired by the T-Scan using the software SA.

In a second step, the cylinder is estimated using Spatial Analyzer.

The resulting radius of the cylinder is shown in Figure 16. In a third step, these processes are identically performed for the 3D point clouds acquired by the s-TLS (Figure 17) and the k-TLS performed with dolly (Figure 18) and rope-slide (Figure 19).

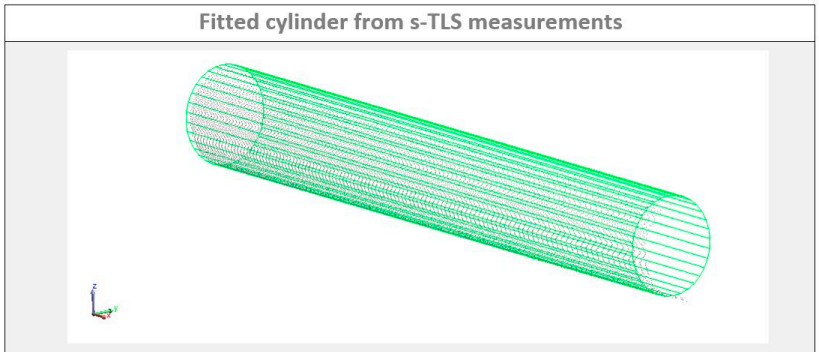

Estimated radius [mm]/ difference to T-Scan [mm]	RMSE [mm]
214.804/ 0.622	1.42
Mutual perpendicular distance [mm]	**Angle between [°]**
0.3	179.98

Figure 17. Estimated cylinder from 3D point clouds acquired by s-TLS using the software Spatial Analyzer compared to estimated cylinder from the 3D point cloud acquired by the T-Scan (radius) and object-to-object relations (cylinder to cylinder/mutual perpendicular distance and angle between).

In a fourth step, the differences between the reference cylinder radius compared to the estimated radius of the different TLS 3D point clouds is calculated (Figures 17–19, marked in red). Additionally, the mutual perpendicular distance and the angle between the estimated cylinders is calculated.

An overview of the results for each configuration is given in Table 6.

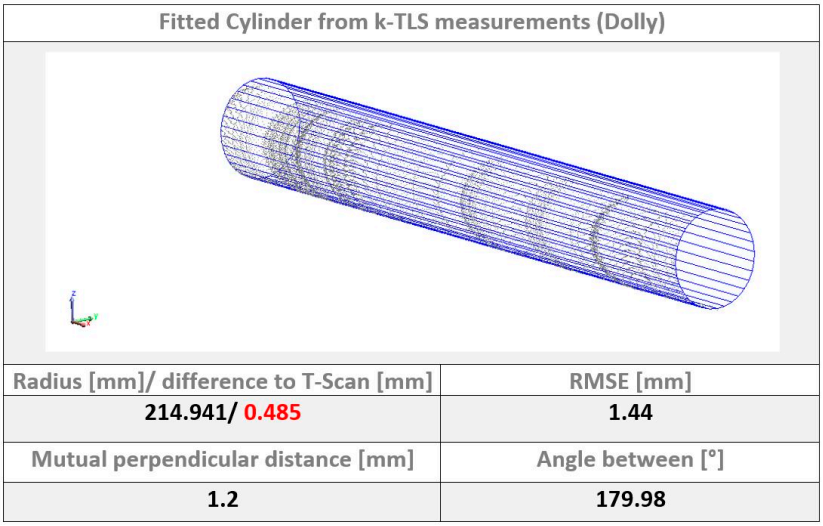

Figure 18. Estimated cylinder from the 3D point cloud acquired by k-TLS with dolly using the software Spatial Analyzer compared to estimated cylinder from the 3D point cloud acquired by the T-Scan (radius) and object-to-object relations (cylinder to cylinder/mutual perpendicular distance and angle between).

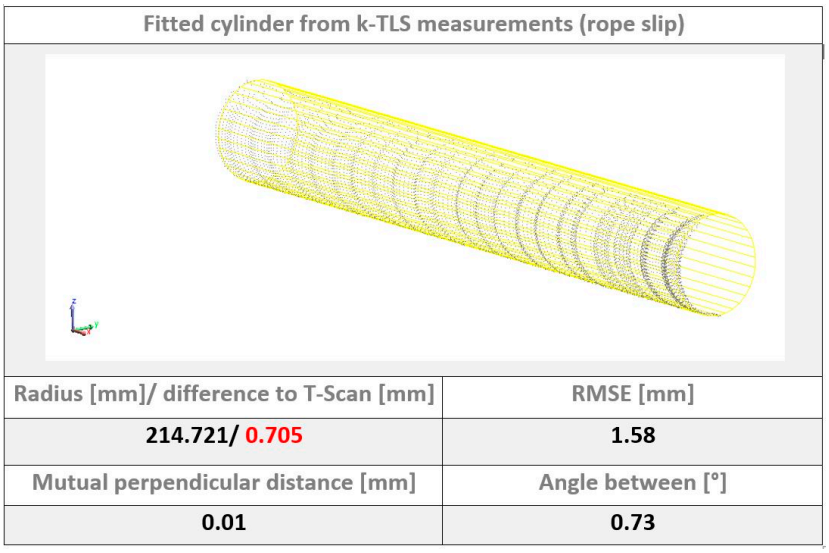

Figure 19. Estimated cylinder from the 3D point cloud acquired by k-TLS with rope-slide using the software Spatial Analyzer compared to estimated cylinder from the 3D point cloud acquired by the T-Scan (radius) and object-to-object relations (cylinder to cylinder/mutual perpendicular distance and angle between).

Table 6. Results of the cylinder comparison with cylinder estimated from T-Scan 3D point cloud as reference data.

Configuration	RMSE [mm]	Estimated Radius [mm]	Difference Radius T-Scan—TLS [mm]	Mutual Perpendicular Distance [mm]	Angle between [°]
T-Scan	1.29	215.43	—	—	—
s-TLS	1.42	214.80	0.62	0.3	179.98 (−0.02)
k-TLS dolly	1.44	214.94	0.49	1.2	179.98 (−0.02)
k-TLS rope-slide	1.58	214.72	0.70	0.01	0.73

5.3.2. Backward Modeling-Direct 3D Point Cloud to 3D Point Cloud Comparison Based on the M3C2 Algorithm

A second approach in forward modeling, based on direct cloud-to-cloud comparison, is presented in this section. This approach is based on the M3C2 algorithm [19,34], which directly calculates the 3D distances between two 3D point clouds. Here, the highly accurate 3D point cloud acquired with the T-Scan is used as a reference. Using the open-source software CloudCompare (cloudcompare.org) [32], the M3C2 distances between the reference 3D point cloud and the 3D point clouds captured with k-TLS (dolly and rope-slide) and s-TLS are calculated. The reference point cloud was used without subsampling, resulting in 2,073,645 core points. For the calculation of the normals, with an estimated diameter of 30, the multi-scale setting was used. Figures 20–25 show the results of this approach.

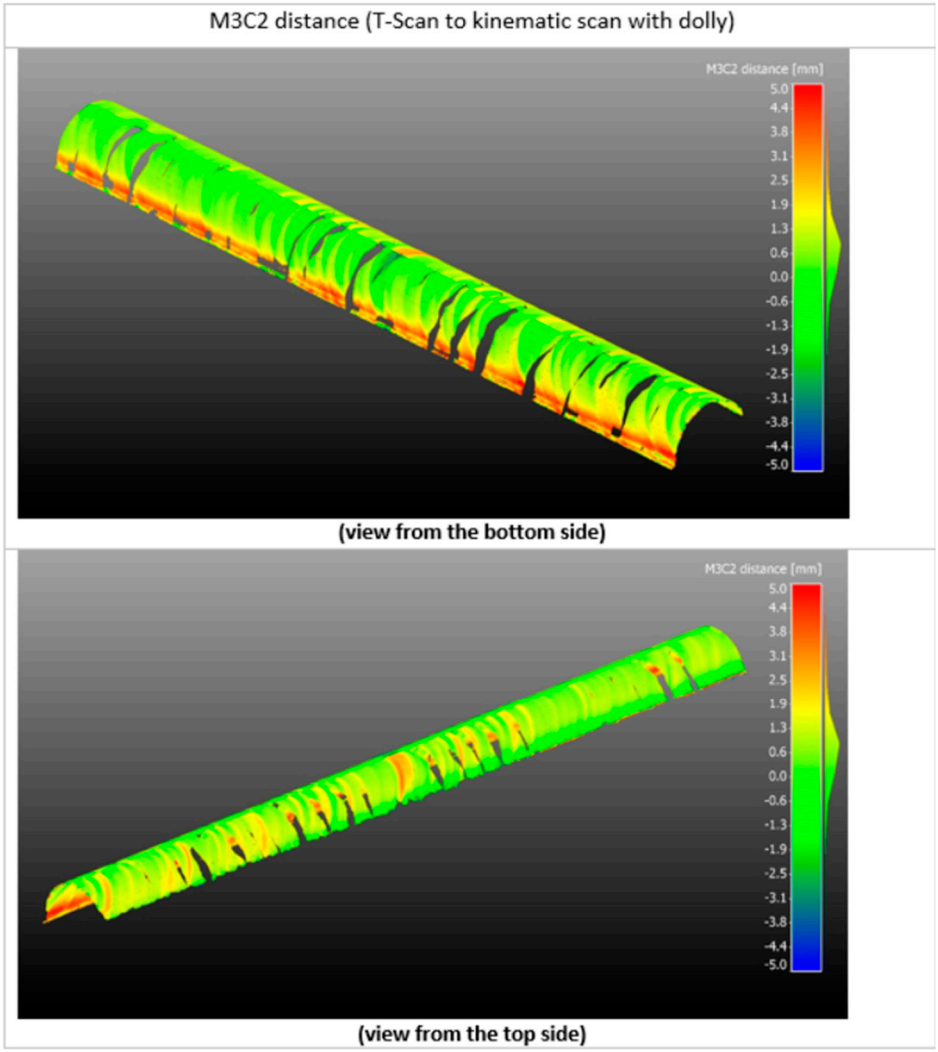

Figure 20. M3C2 distances of two 3D point clouds (reference point cloud and k-TLS carried by dolly) showing the cylindrical part (top left: view from the bottom, bottom left: view from the top) of the mock-up (Figure 11).

The resulting M3C2 distances for the 3D point cloud acquired by the T-Scan and the 3D point cloud acquired by the k-TLS-based MSS using the dolly are shown in Figure 20. The distribution of the M3C2 distances are shown in Figure 21. Due to the position of the sensors center, which was located slightly above the cylindrical structure, the areas in the lower part have the largest deviations. The reason lies in the very flat vertical angle of incidence and possible multi reflections [1], which also

contribute to the deviations in the upper region of the structure. As expected, the best results are in the center of the structure, since both the vertical and horizontal angle of incidences are close to 90°.

Approximately 87% of the calculated M3C2 distances are in the range of −2 mm to +2 mm. The maximum is located at +0.75 mm. This shift to the right can be explained by the position of the sensor center, which is not concentric to the mock-up.

The resulting M3C2 distances for the 3D point cloud acquired by the T-Scan and the 3D point cloud acquired by the k-TLS-based MSS using the rope-slide are shown in Figure 22. The distribution of the M3C2 distances is shown in Figure 23.

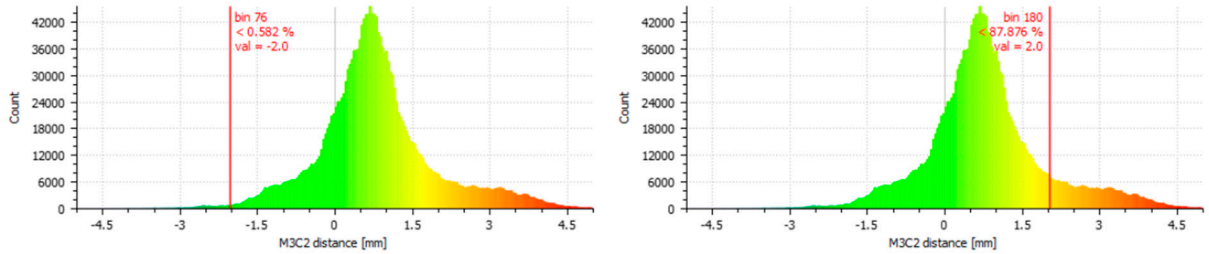

Figure 21. Histogram of M3C2 distances for the comparison of the 3D point clouds acquired by the T-Scan and the k-TLS-based MSS using the dolly.

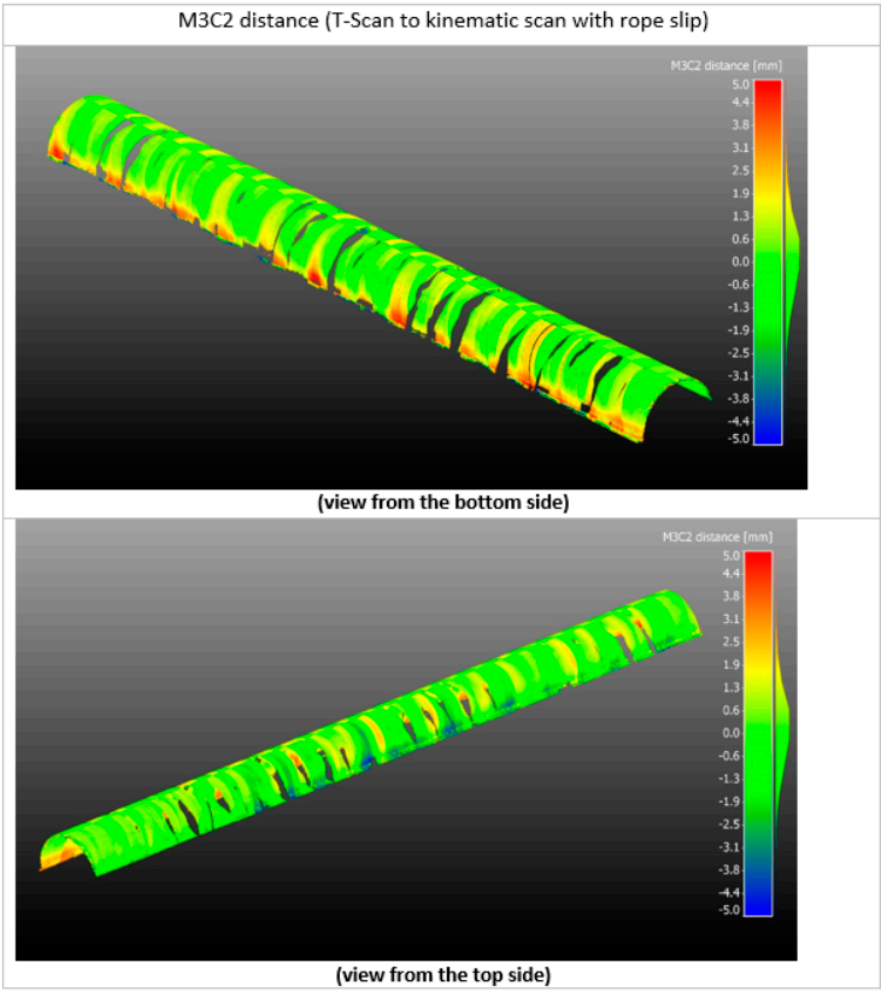

Figure 22. M3C2 distances of two 3D point clouds (reference point cloud and k-TLS carried by rope-slide) showing the cylindrical part (top left: view from the bottom, bottom left: view from the top) of the mock-up (Figure 11).

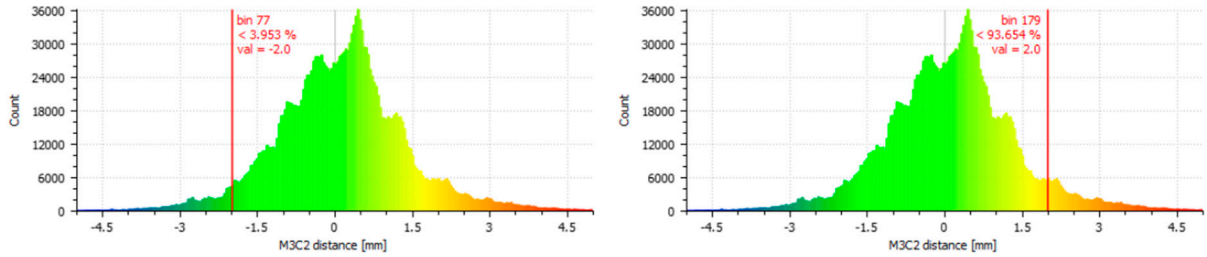

Figure 23. Histogram of M3C2 distances for the comparison of the 3D point clouds acquired by the T-Scan and the k-TLS-based MSS using the rope-slide.

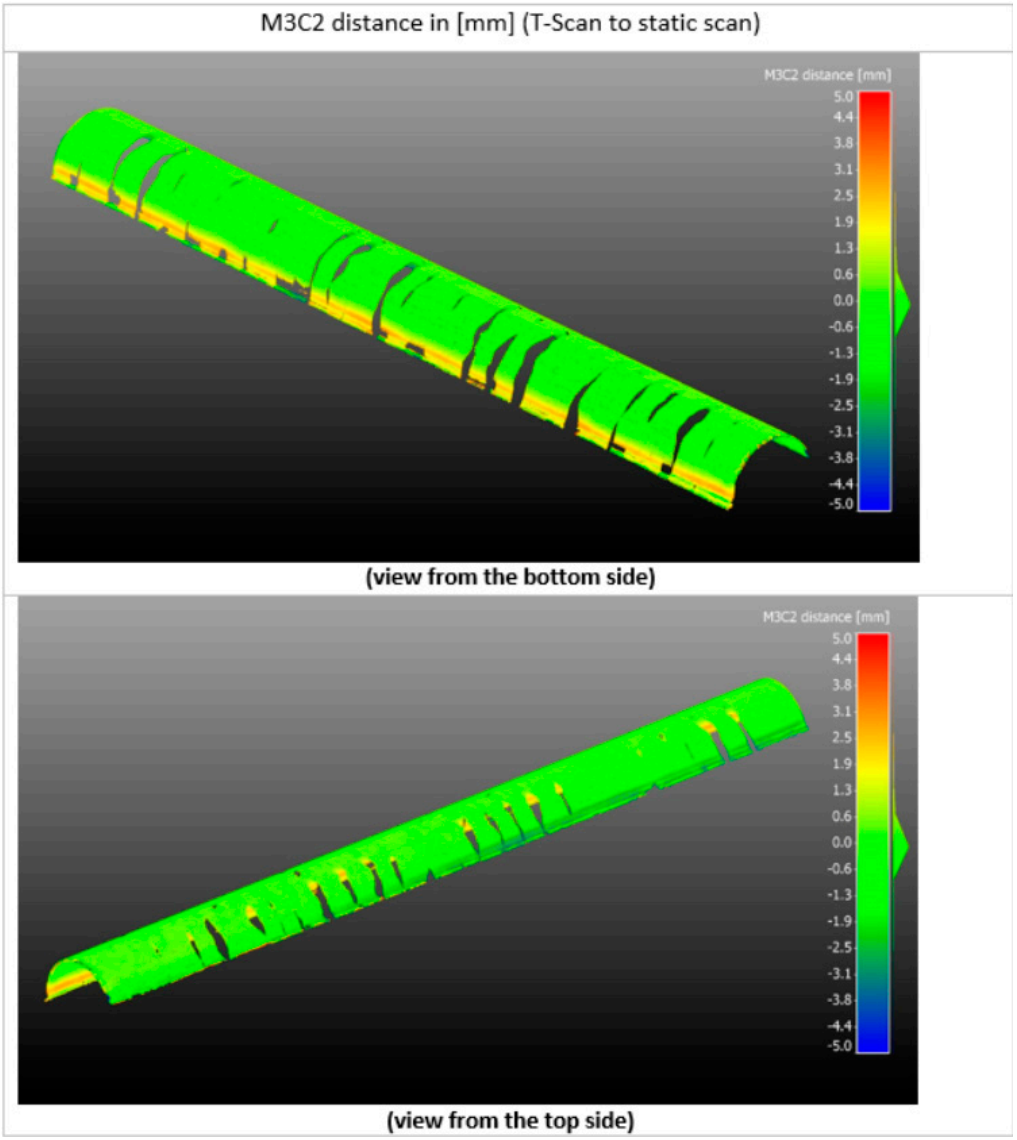

Figure 24. M3C2 distances of two 3D point clouds (reference point cloud and s-TLS) showing the cylindrical part (top left: view from the bottom, bottom left: view from the top) of the mock-up (Figure 11).

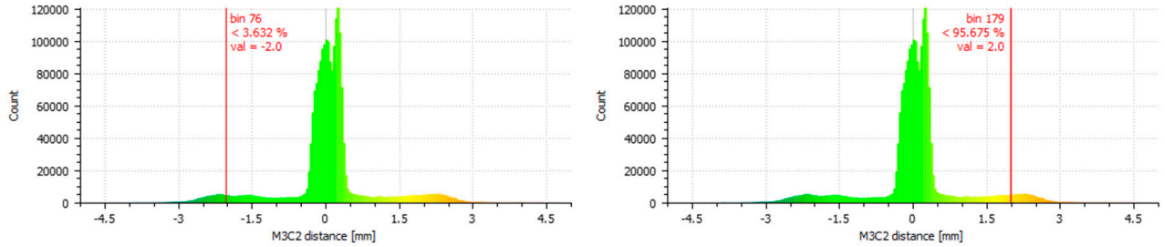

Figure 25. Histogram of M3C2 distances for the comparison of the 3D point clouds acquired by the T-Scan and by the s-TLS.

Again, approximately 89.5% of the calculated M3C2 distances are in the range of −2 mm to +2 mm. The maximum of the histogram is located at +0.5 mm (Figure 21). The largest deviations, resulting from the flat vertical angle of incidence and possible multi reflection, can be found at the top and bottom of the cylindrical structure, as well. Maximum deviations are ±5 mm.

The resulting M3C2 distances for the 3D point cloud acquired by the T-Scan and the 3D point cloud acquired by s-TLS are shown in Figure 24. The distribution of the M3C2 distances is shown in Figure 25.

Approximately 92% of the calculated M3C2 distances are in the range of −2 mm to +2 mm. The maximum of the histogram is located at +0.25 mm (Figure 25). The largest deviations, resulting from the flat vertical angle of incidence, can also be found at the top and bottom of the cylindrical structure. Due to the positioning of the sensor at the vertical center of the cylindrical structure, the differences at the top and the bottom are equal and only a slight shift to the right is visible. The maximum deviations are ±3 mm.

In the following, the investigations of the M3C2 distances for the entire mock-up will be presented. Figures 26 and 27 show the M3C2 distances for T-Scan and k-TLS with the dolly as the sensor platform.

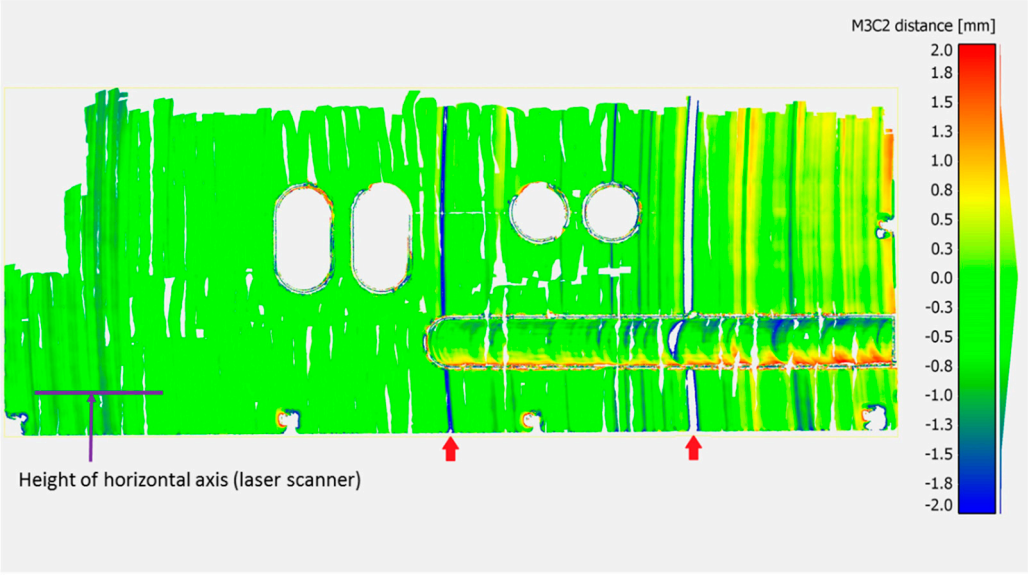

Figure 26. Frontal view of the mock-up showing the M3C2 distances of the 3D point clouds captured with the T-Scan and k-TLS (dolly). The legend on the right side shows the histogram and the magnitude of the M3C2 differences. Profiles with lower accuracy, resulting from joints on the floor, are marked with red arrow.

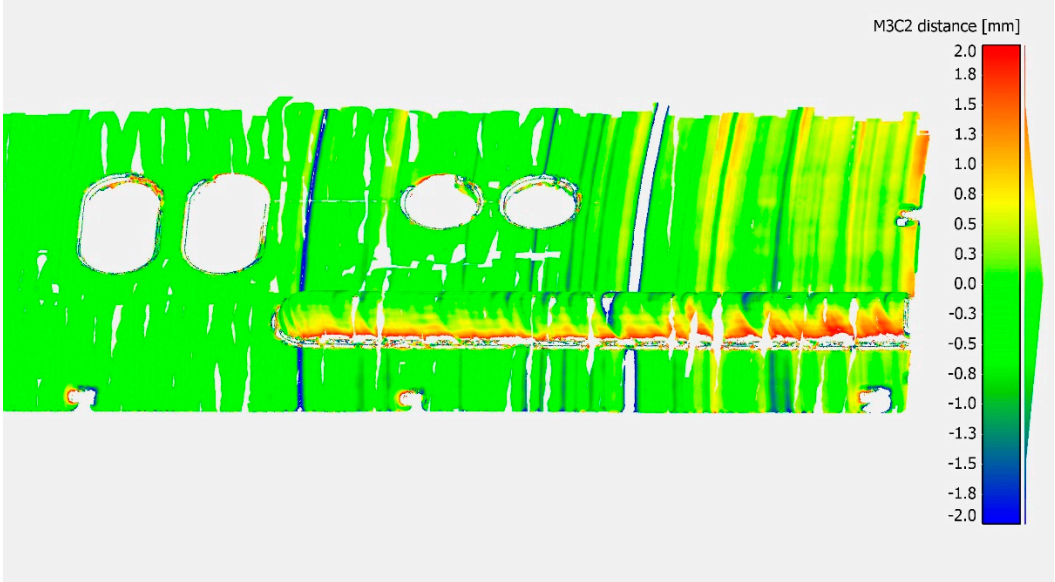

Figure 27. Bottom view on the mock-up showing the M3C2 distances of the 3D point clouds captured with the T-Scan and k-TLS (dolly).

With increasing distance, a constant increase of the M3C2 distances up to 0.6 mm is observed. The previously described influence of the angle of incidence and multi reflection on the cylindrical structure is also visible at the edges of the portholes (Figure 27). Joints on the floor, resulting in small jumps of the dolly, lead to laser scan profiles with lower accuracy (Figures 26 and 28, marked with red arrows).

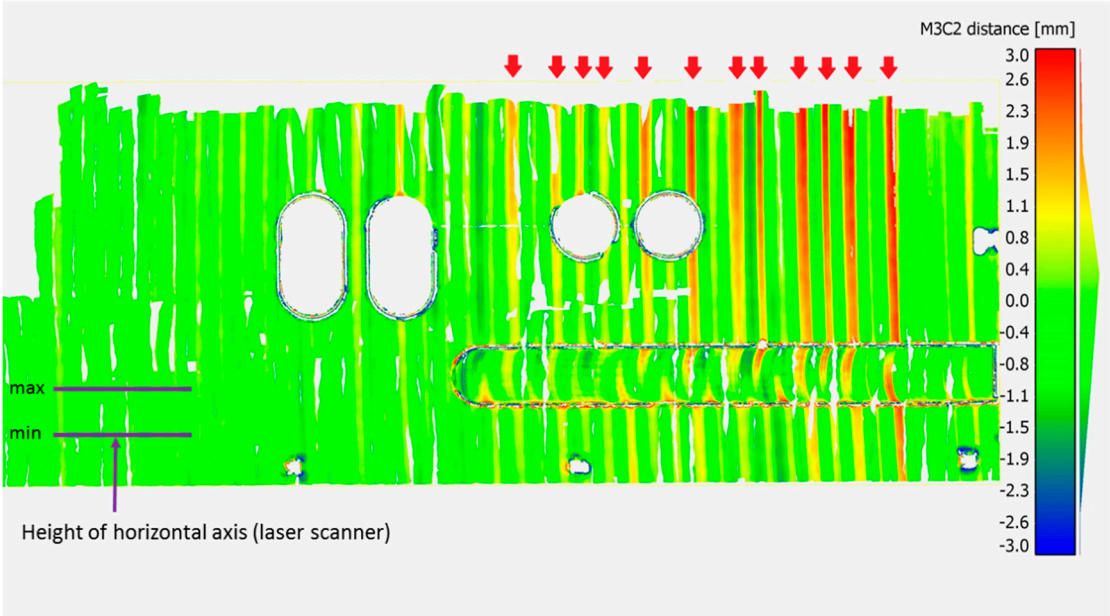

Figure 28. Frontal view on the mock-up showing the M3C2 distances of the 3D point clouds captured with the T-Scan and k-TLS (rope-slide). The legend on the right side shows the histogram and the magnitude of the M3C2 differences. Differences resulting from pendulum movement of the laser scanner are marked by red arrows.

Figures 28 and 29 show the M3C2 differences for the T-Scan and k-TLS with the rope-slide as the sensor platform. The constant accelerated movement is taken into account within an iterative extended Kalman Filter (iEKF). During the experiment, an unstable suspension of the laser scanner on the rope-slide was used. This results in a swinging or pendulum movement of the laser scanner.

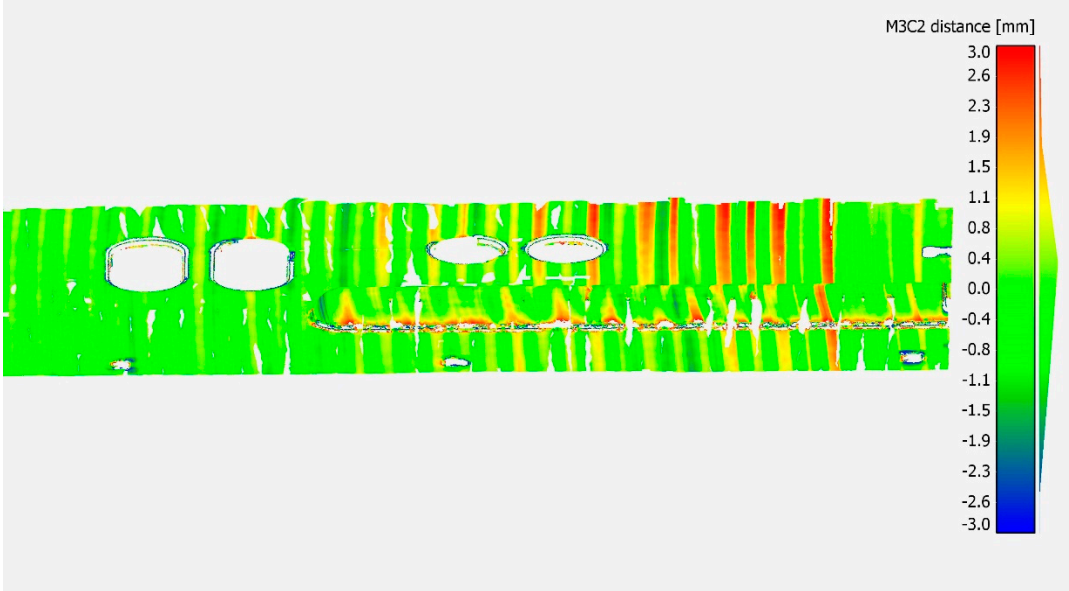

Figure 29. Bottom view on the mock-up showing the M3C2 distances of the 3D point clouds captured with the T-Scan and k-TLS (rope-slide).

The pendulum movement is not sufficiently considered in the iEKF, this leads to increasing M3C2 distances up to ~3 mm, depending on the amplitude of the pendulum motion (Figure 28, marked by red arrows).

The influences of a flat vertical angle of incidence and possible multi reflection can be seen at the bottom and top of the cylindrical structure (Figure 29).

Figures 30 and 31 show the M3C2 differences for the T-Scan and s-TLS. The s-TLS standpoint was concentric in front of the mock-up within a distance of approximately 4 m.

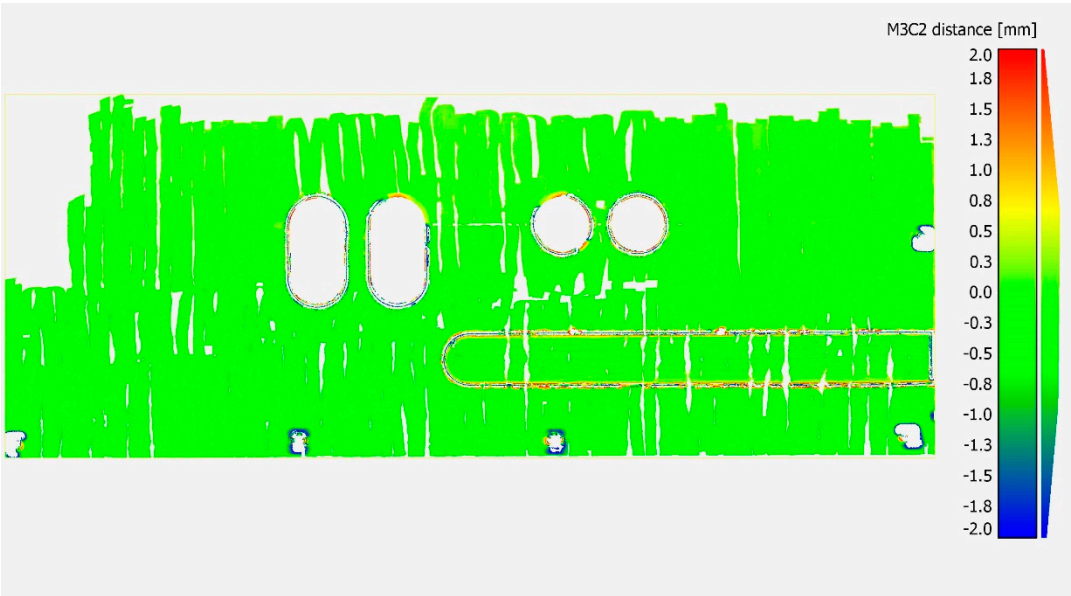

Figure 30. Frontal view on the mock-up showing the M3C2-distances of the 3D point clouds generated with the T-Scan and s-TLS.

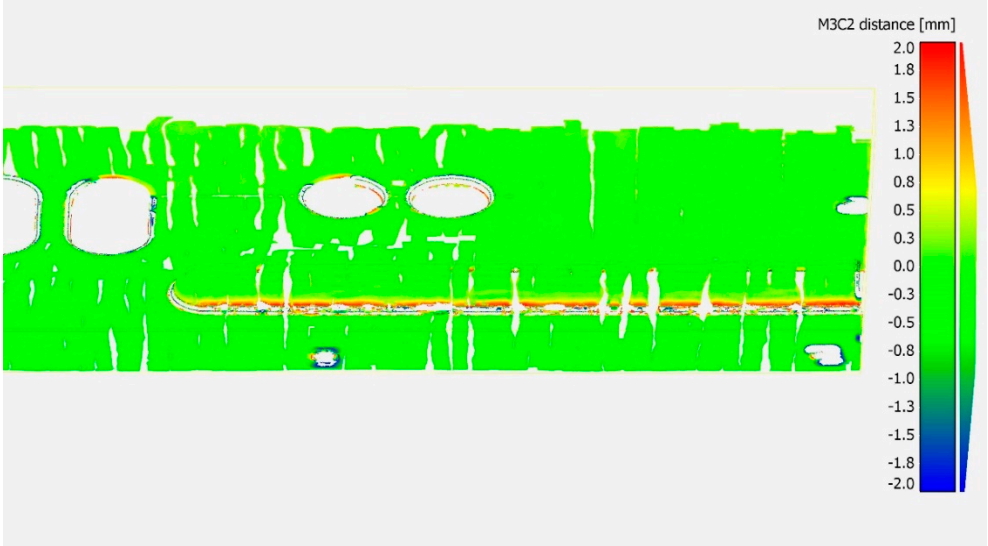

Figure 31. M3C2 distances of the 3D point clouds captured by the T-Scan and s-TLS showing a bottom view of the cylindrical structure.

Within this short distance and a nearly perpendicular horizontal and vertical angle of incidence, only small differences in the M3C2 distances are recognizable. At the center of the mock-up, differences are ±0.0 mm. With slightly increasing distance and, therefore, angles of incidence, the M3C2 distances increase up to +0.2 mm at the top-right and -left corner and −0.5 mm at the bottom-left and -right corner (Figure 30). Only areas with a flat angle of incidence show larger deviations from ±2 mm at the bottom and top of the cylindrical structure and the edges of the portholes (Figure 31).

An overview of the deviations and distributions for each of the three described 3D point clouds acquisition approaches is given in Figure 32. For each approach, an upper and lower border for the histogram of the M3C2 distances is presented:

- For the comparison of the T-Scan and the dolly-carried k-TLS, 97% of the M3C2 distances are within a range of −1.5 mm to +1.0 mm, with a histogram equal to the normal distribution and the maximum shifted to the left (−0.3 mm);
- For the comparison of the T-Scan and the rope-slide-carried k-TLS, 94% of the M3C2 distances are within a range of −1.5 mm to +1.5 mm, with a histogram equal to the normal distribution and the maximum shifted to the left (−0.3 mm);
- For the comparison of the T-Scan and the s-TLS, 95% of the M3C2 distances are within a range of −0.5 mm to +0.2 mm, with a histogram equal to the normal distribution and a maximum shifted slightly to the left (−0.1 mm). A second maximum can be found at −0.3 mm.

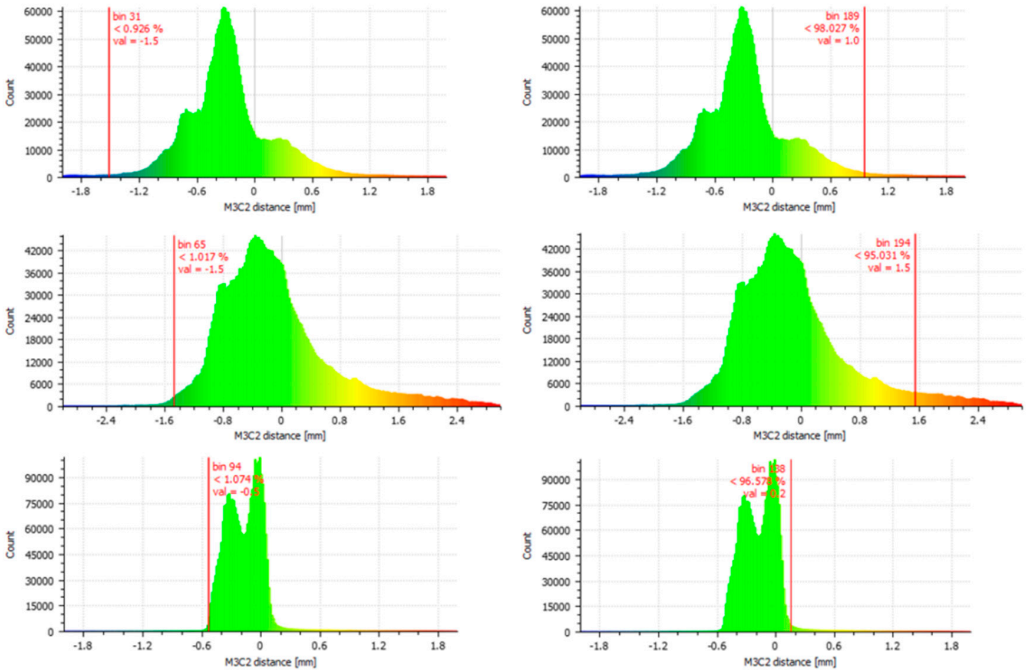

Figure 32. Histogram of M3C2 distances [mm] for the entire mock-up (top-left and -right: T-Scan to k-TLS with dolly; middle-left and -right: T-Scan to k-TLS with rope-slide; bottom-left and -right: T-Scan to s-TLS.

5.3.3. Forward Modeling with the Intensity-Based Approach

Based on the recorded intensity values, the forward modeling was processed using the described stochastic model in Section 3.2. This approach is carried out for the k-TLS carried by dolly (Figure 33), the k-TLS carried by rope-slide (Figure 34) and the s-TLS (Figure 35). These three figures provide a visual overview of the results, processing the 3D Helmert point error for each scanned point, see Equation (5). The legend on the right side of each figure provides the values and the histogram of the 3D point errors. These values contain only the accuracy of the scanned points, the influences resulting from reference framework, (geo-) referencing, system calibration and synchronization are not yet considered therein.

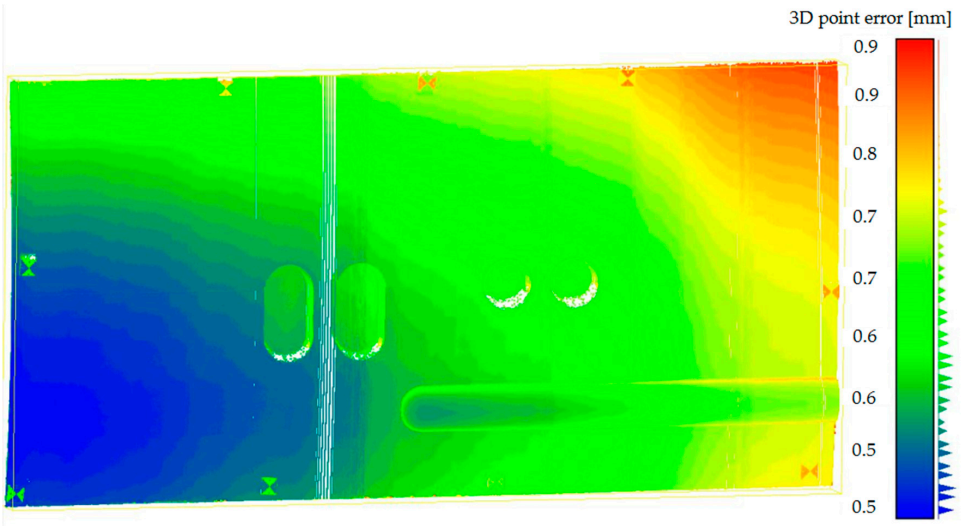

Figure 33. The 3D point error in [mm] derived from the intensity values of the 3D point cloud captured by k-TLS at the mock-up (sensor platform: dolly, trajectory: 45° in relation to the mock-up, distance: ~3 m at the right, ~5 m at the left).

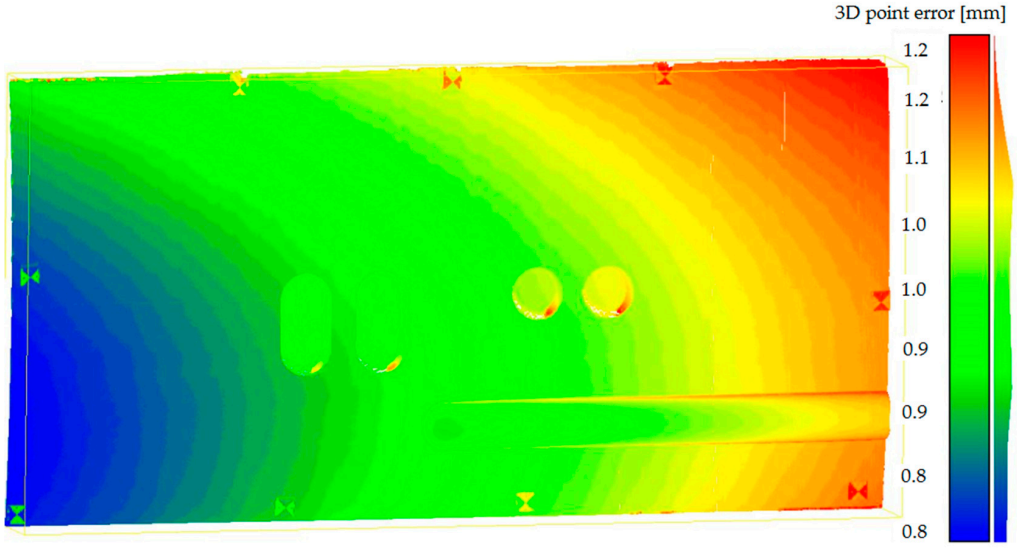

Figure 34. 3D point error in [mm] derived from the intensity values of the 3D point clouds captured by k-TLS at the mock-up (sensor platform: rope-slide).

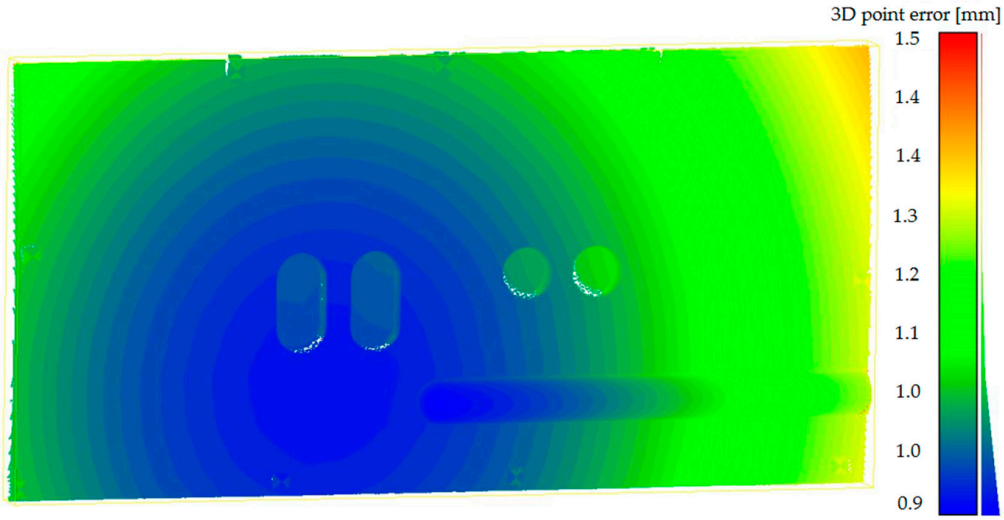

Figure 35. The 3D point error in [mm] derived from the intensity values of the 3D point cloud captured by s-TLS at the mock-up (distance: ~5 m).

For the experiment performed with the k-TLS-based MSS using the dolly, the 3D point error of the 3D point cloud lies in a range of 0.5 mm to 0.9 mm. The trajectory of the k-TLS-based MSS is within an angle of 45° in relation to the mock-up, resulting in an increasing horizontal distance in the direction of movement (3 m to 5 m) and an increasing vertical distance at the bottom and top of the mock-up in relation to the center of the laser scanner. The vertical angle of incidence increases upwards and downwards in relation to the center of the laser scanner. The horizontal angle of incidence is constant for each scanned profile at 90°. The dolly was moved with nearly constant speed (mean 0.13 m/s). Higher deviations at the edges of the porthole and the cylindrical structure result from the flat angle of incidence and multiple reflections are also visible.

The histogram of the 3D point error is elliptical around the sensor center at the shortest horizontal distance. The increasing distance from the sensor center to the mock-up results in the increasing standard deviations in the direction of movement. In the upper- and lower-part of the mock-up, the longer slope distances and the influence of the vertical angle of incidence adds to the longer horizontal distance.

For the experiment performed with the k-TLS-based MSS using the rope-slide, the 3D point errors of the point cloud are in a range of 0.8 mm to 1.2 mm (Figure 34). The trajectory of the k-TLS-based MSS is inclined to the mock-up within a horizontal distance of 4 m at the beginning, up to 5 m at the end. The vertical distance increases at the bottom and top of the mock-up in relation to the center of the laser scanner. The vertical angle of incidence increases upwards and downwards in relation to the center of the laser scanner, which is moving downwards in the direction of movement. The horizontal angle is constant for each scanned profile at around 90°. The k-TLS-based MSS using the rope-slide was uniformly accelerated with up to a maximum speed of 1 m/s in the direction of movement.

The distribution of the 3D point error is elliptical around the sensor center at the lowest speed. The increasing speed leads to an increasing standard deviation in the direction of movement. In the upper- and lower-part of the mock-up, the longer slope and vertical distance and the influence of the vertical angle of incidence add up to the deviations resulting from the acceleration of the movement. Higher deviations at the edges of the porthole and the cylindrical structure result from the flat angle of incidence and multiple reflections are also visible.

For the measurements performed with the s-TLS, the 3D point error, as a parameter for the accuracy of the 3D point cloud, is settled in a range of 0.9 mm to 1.5 mm (Figure 35). However, more than 90% of the calculated point errors are within the range of 0.9 mm to 1.0 mm. Higher standard deviations at the edges of the porthole and the cylindrical structure result from the flat angle of incidence and multiple reflections are also visible. The histogram of the 3D point errors is nearly circular around the sensor's center. The horizontal distance (sensor center to mock-up) is approximately 4 m. Higher deviations in the corners are the result of longer slope distances.

5.3.4. Forward Modeling-with Additional Influences for the s- and k-TLS Measurements

In addition to the 3D point error, further effects must be considered. These effects are specified in Section 4.2. For the following considerations, the assumption is made that all influences are independent and, therefore, the combined standard deviation of s-TLS is achieved by

$$\sigma_{s-TLS} = \sqrt{\sigma_{ref.}^2 + \sigma_{stat.LS}^2 + \sigma_{xyz}^2} \quad (8)$$

With the following standard deviations:

$\sigma_{ref.}$ = determination of the reference framework;
$\sigma_{stat.LS}$ = (geo-) referencing of the laser scanner in the reference framework;
σ_{xyz} = 3D point error (based on intensity values).

In Table 7, an assessment of the (total) uncertainty for the s-TLS is shown. The minimum and maximum distance d_{LS} of the 3D object acquisition was chosen here to show the distance dependency.

Table 7. Exemplary assessment of the (total) uncertainty of the s-TLS.

Platform	d_{LS} [m]	$\sigma_{ref.}$ [mm]	$\sigma_{stat\ LS}$ [mm]	σ_{xyz} [mm]	σ_{k-TLS} [mm]
s-TLS (min)	5	0.1	0.3	0.9	0.95
s-TLS (max)	6			1.3	1.34

For k-TLS the combined standard deviation is calculated as

$$\sigma_{k-TLS} = \sqrt{\sigma_{ref.}^2 + \sigma_{stat.LT}^2 + \sigma_{(geo-)\ ref.}^2 + \sigma_{syst.calib.}^2 + \sigma_{xyz}^2} \quad (9)$$

with the following standard deviations:

$\sigma_{ref.}$ = determination of the reference framework;
$\sigma_{stat.\ LT}$ = (geo-) referencing of the LT in the reference framework;

$\sigma_{(geo-)\ ref.}$ = (geo-) referencing of the platform;
$\sigma_{syst.calib.}$ = system calibration;
σ_{xyz} = 3D point error (based on intensity values).

In Table 8, an assessment of the (total) uncertainty budget for the k-TLS is shown. There, the following standard deviations $\sigma_{rot} = 0.002°$ are used for the rotations of the (geo-) referencing, as well as for the system calibration. Furthermore, the minimum and maximum distance (d_{LT}) for the (geo-) referencing and (d_{LS}) for the 3D object acquisition were used to show the range of the different uncertainty components.

Table 8. Exemplary assessment of the (total) uncertainty of the k-TLS.

Platform	d_{LT} [m]	d_{LS} [m]	$\sigma_{ref.}$ [mm]	$\sigma_{stat\ LT}$ [mm]	$\sigma_{(geo-)\ ref.}$ [mm]		$\sigma_{syst.\ calib.}$ [mm]		σ_{xyz} [mm]	σ_{k-TLS} [mm]
					$\sigma_{t_x\ t_y\ t_z}$	$\sigma_{rot.}$	$\sigma_{t_x\ t_y\ t_z}$	$\sigma_{rot.}$		
dolly (min)	2	3	0.1	0.16	0.011	0.10	0.1	0.15	0.5	0.59
dolly (max)	8.5	5			0.033	0.42		0.25	0.9	1.06
rope-slide (min)	5.5	4			0.024	0.27		0.20	0.8	0.90
rope-slide (max)	10	6			0.038	0.49		0.30	1.2	1.36

6. Results and Conclusions

Based on the question of whether the achievable accuracies using of s-TLS- and k-TLS-based MSS make it possible, or appropriate, to be used in an industrial environment, an evaluation of the presented results is carried out in this section. This includes, on the one hand, the discussion and the assessment of the attained accuracies and the evaluation approaches, while on the other hand, an outlook on possible improvements regarding the used procedures. Here, both the measurement itself and the evaluation methods should be considered.

6.1. Discussion of the Results

In the following sections, the suitability of s-TLS- and k-TLS-based MSS should be discussed. The main aspect is the attainable accuracy of both systems and if they meet the requirements of industrial surveying applications.

6.1.1. Backward Modeling—Calculation of Geometric Parameters

Previous laboratory studies [22] have shown that geometric parameters of reference structures can be estimated with an RMS of 0.1–0.2 mm for different kinds of objects, including a cylindrical structure, with a measurement set-up consisting of LT and T-Scan. As shown in Table 6, the cylindrical structure of the mock-up is captured by T-Scan with an RMS of 1.3 mm, which suggests that this is not an ideal cylinder. Indeed, all presented measurement set-ups show comparable results with RMS from 1.4 mm to 1.6 mm, which is close to the T-Scan measurement results. For all set-ups, the difference of the calculated radius to the estimated radius from the T-Scan 3D point cloud, is better than ±1 mm (0.5–0.7 mm). All influences (3D point cloud acquisition by TLS, synchronization, registration and (geo-) referencing) are included here.

6.1.2. Backward Modeling—M3C2 Distances

For a direct comparison of the captured TLS 3D point clouds to a reference 3D point cloud captured by the T-Scan, the M3C2 algorithm is used. For all measurement set-ups, the M3C2 differences for planar surfaces are better than ±1 mm for measuring distances up to 5 m. For measurement distances up to 10 m, M3C2 distances of better than ±2 mm are attainable. Objects captured with a flat angle of incidence, like the bottom and top of the cylindrical structure or the portholes, show significantly higher deviations (3–5 mm), see Figures 26–31. To avoid these deviations, additional standpoints (s-TLS) or a

different alignment of the platform (k-TLS) with a better angle of incidence, are necessary. In the case of the k-TLS-based MSS carried by dolly, larger bumps on the ground lead to higher standard deviations, see Figures 26 and 27. For the k-TLS-based MSS carried by the rope-slide higher M3C2 distances, up to 3 mm, are visible, see Figures 28 and 29. This occurs mainly in the initial phase of the measurements during the strongest acceleration of the k-TLS-based MSS. Due to the simple suspension, vibrations have been transmitted to the carrier, resulting in slightly oscillating movements.

6.1.3. Forward Modeling

The intensity-based approach shows comparable results for all three experiments. For distances up to 5 m, 3D point errors better than 1 mm are achieved. Objects captured with a flat angle of incidence, like the bottom and top of the cylindrical structure or the portholes, show significantly higher point errors.

The dolly carried k-TLS-based MSS shows the smallest combined 3D standard deviations at a measuring distance to the object of 2 m and a (geo-) referencing distance of 3 m, see Table 8. Here, a 3D Helmert point error of 0.5 mm and a combined standard deviation of 0.6 mm considering the additional effects of (geo-) referencing, system calibration, stationing of the LT and reference frame is obtained. With a combined standard deviation of 1.4 mm, the largest values are obtained for the k-TLS-based MSS carried by the rope-slide. Here, the (geo-) referencing distance was 10 m and the distance to the object was 6 m. For this k-TLS realization, it must be noted that the rotations of the (geo-) referencing, as well as for the system calibration, need to be determined very accurately. It can be seen in the forward modeling, that in both cases—(geo-) referencing and system calibration—an accuracy of the rotations of 0.001–0.002 has to be attained to ensure an object capturing with a combined 3D standard deviation of 1–2 mm. Because of the distance dependency, the influence of the rotations is increasing. For the s-TLS, with fewer influencing factors, the combined standard deviation increases from ~1.0 mm at a distance to the object of 5 m and to 1.35 mm at a distance of 6 m. Here, it has to be stated that the most important impact comes from the 3D object capturing.

6.2. Classification and Assessment of the Results

In this contribution, it was shown that all measurements and processing methods, which were carried out in a laboratory [22], could be transferred into a larger industrial environment. A crucial role is taken over by the distance measurement. Investigations presented in [8,37] show that the influences resulting from the angle of incidence are of secondary importance (a significant influence occurs at angles of incidence between 0° and 20°). Flat angles of incidence leading to multiple reflections, which must be taken into account. For efficient data acquisition, the measurement set-up should be adapted to the required accuracies. If the required accuracies are ~1 mm, the measuring distance should not exceed 5 m. With required accuracies of ±2 mm, even larger distances (8 m) are conceivable. Considering the small accuracy differences between s- and k-TLS, the use of k-TLS-based MSS is recommended. Especially for large objects with restricted conditions, e.g., small field of view, the number of standpoints increases for s-TLS. Here, the use of a k-TLS-based MSS is even more beneficial. In principle, all three methods are suitable for 3D object capturing, with a standard deviation of ~1 mm for a single 3D point of the 3D point cloud. In an industrial environment, the combination s-TLS and k-TLS will provide the most options to the operator.

6.3. Outlook

TLS has already proven its potential in industrial surveying. The present work shows some aspects of quality assessment of s- and k-TLS captured data sets. The forward modeling is currently only carried out by a simplified assumption that the individual processes are independent and that there are no correlations. However, this should be improved in future work, since, e.g., the uncertainties of the reference points affect the stationing of the laser scanner (s-TLS) and the LT (k-TLS).

For future work, these interdependencies should be taken into account in the determination of the total uncertainty budget.

For the dolly-carried k-TLS-based MSS, the use of damping elements is what is aimed for. This should also be applied to the rope-slide-based solution. Further, an improved suspension and a motor control should be realized. This will lead to a uniformly accelerated motion and suppressed pendulum motions. It can be summarized that a k-TLS-based MSS carried by a rope-slide promises the best alternative with sufficient accuracy and flexibility. For industrial production with high-accuracy requirements ($\sigma_{3D} = 1$ mm), the quality analysis of the captured 3D point clouds is of particular importance. A possible future application of the proposed k-TLS-based MSS is the 3D capturing of elongated objects of several tens up to hundreds of meters, e.g., aircrafts, ships, trains and wind energy turbines.

Author Contributions: U.S. wrote main parts of the paper, analyzed the data and performed the 3D point cloud acquisition with s-TLS. J.H. performed the 3D point cloud acquisition with the k-TLS-based MSS, provided and analyzed parts of the data for the k-TLS and contributed several sections related to k-TLS. J.-A.P. supported with consultations in particular to s-TLS and general MSS topics as well as proof-reading of the manuscript. I.N. supported with consultations. All authors reviewed the manuscript. All authors have read and agreed to the published version of the manuscript.

Funding: Some results of this contribution were obtained in a cooperation project sponsored by the VDI/VDE as project (16KN035225) and further results of the collaborative research project "FINISH—Exakte und schnelle Geometrieerfassung sowie Datenauswertung von Schiffsoberflächen für effiziente Beschichtungsprozesse" and part of the subproject "Entwicklung von Algorithmen und Qualitätsprozessen für ein neuartiges kinematisches terrestrisches Laserscanningsystem (03SX406D)". Both projects were funded by the German Federal Ministry for Economic Affairs and Energy (BMWi). The publication of this article was funded by the Open Access fund of Leibniz Universität Hannover.

Acknowledgments: All authors would like to acknowledge the project partners for their helpful assistance within the extensive measurements. The authors also thanks the project partner DHPI for providing the T-Scan measurement data.

Conflicts of Interest: The authors declare no conflict of interest.

References

1. Gordon, B. Determining the Uncertainties Concerning Terrestrial Laser Scanner Measurements. Ph.D. Thesis, Technische Universität Darmstadt, Darmstadt, Germany, 2008.
2. Schulz, T.; Ingensand, H. Terrestrial laser scanning—Investigations and applications for high precision scanning. In Proceedings of the FIG Working Week 2004, Athens, Greece, 22–27 May 2004.
3. Kauker, S.; Schwieger, V. First investigations for a synthetic covariance matrix for monitoring by terrestrial laser scanning. In Proceedings of the 3rd Joint International Symposium on Deformation Monitoring (JISDM) 2016, Vienna, Austria, 30 March–1 April 2016.
4. Neitzel, F. Unterssuchung des Achssystems und des Taumelfehlers terrestrischer Laserscanner mit tachymetrischem Messprinzip. In *Terrestrisches Laser-Scanning (TLS 2006), Proceedings of the Beiträge zum 72. DVW-Seminar, Fulda, Germany, 9–10 November 2006*; Schäfer, M., Ed.; Arbeitskreis 4 Ingenieurgeodäsie; Arbeitskreis 3 Messmethoden und Systeme; DVW—Gesellschaft für Geodäsie Geoinformation und Landmanagement e.V.: Augsburg, Germany, 2006.
5. Neitzel, F. Gemeinsame Bestimmung von Ziel-, Kippachsenfehler und Exzentrizität der Zielachse am Beispiel des Laserscanners Zoller + Fröhlich Imager 5003. In *Photogrammetrie—Laserscanning—Optische 3D-Messtechnik*; Wichmann: Oldenburg, Germany, 2006.
6. Schneider, D. Geometriche und Stochastische Modelle für die Integrierte Auswertung Terrestrischer Laserscannerdaten und Photogrammetrischer Bilddaten. Ph.D. Thesis, Technical University of Dresden, Dresden, Germany, 2008.
7. Soudarissanane, S.; Lindenbergh, R.; Menenti, M.; Teunissen, P.J.G. Scanning geometry: Influencing factor on the quality of terrestrial laser scanning points. *ISPRS J. Photogramm. Remote Sens.* **2011**, *66*, 389–399. [CrossRef]

8. Zámečníková, M.; Neuner, H. Der Einfluss des Auftreffwinkels auf die reflektorlose Distanzmessung. In *Terrestrisches Laserscanning 2014 (TLS 2014), Proceedings of the Beiträge zum 139. DVW-Seminar, Fulda, Germany, 11–12 Dezember 2014*; DVW—Gesellschaft für Geodäsie, Geoinformatik und Landmanagement e.V., Ed.; DVW—Gesellschaft für Geodäsie Geoinformation und Landmanagement e.V.: Augsburg, Germany, 2014.
9. Neitzel, F.; Neumann, I. Scanning in Motion—Kinematisches TLSmittels mobiler Plattformen. In *Terrestrisches Laserscanning 2012 (TLS 2012), Proceedings of the Beiträge zum 121. DVW-Seminar, Fulda, Germany, 13–14 Dezember 2012*; DVW e.V.: Augsburg, Germany, 2013.
10. Leica Geosystems AG. Leica ProScan Data Sheet. Available online: https://leica-geosystems.com/en-gb/products/mobile-sensor-platforms/capture-platforms/leica-proscan (accessed on 26 November 2018).
11. Applanix Corporation. TIMMS: Fast, Accurate & Cost-Effective Indoor Mapping. Available online: https://www.applanix.com/products/timms-indoor-mapping.htm (accessed on 29 November 2018).
12. ViAmetris. IMS3D Data Sheet. Available online: http://www.viametris.com/products/ims3d/ (accessed on 29 November 2018).
13. Keller, F. *Entwicklung eines Forschungsorientierten Multi-Sensor-Systems zum Kinematischen Laserscanning Innerhalb von Gebäuden*; Shaker Verlag: Aachen, Germany, 2016.
14. Kukko, A. Mobile Laser Scanning—System Development, Performance and Applications. Liikkuva Laserkeilaus—Järjestelmäkehitys, Suorituskyky ja Sovellukset. Ph.D. Thesis, Aalto University, Tampere, Finland, 2013.
15. Heinz, E.; Eling, C.; Wieland, M.; Klingbeil, L.; Kuhlmann, H. Development of a Portable Mobile Laser Scanning System with Special Focus on the System Calibration and Evaluation. In Proceedings of the 5th International Conference on Machine Control and Guidance (MCG), Vichy, France, 5–6 October 2016.
16. 3D Mapping Solutions. KiSS®(Kinematic Survey System) und MoSES (Mobiles Straßen Erfassungs-System). Available online: http://www.3d-mapping.de (accessed on 26 November 2018).
17. Wujanz, D. Terrestrial Laser Scanning for Geodetic Deformation Monitoring. Ph.D. Thesis, Technische Universität Berlin, Berlin, Germany, 2016.
18. Wujanz, D.; Burger, M.; Mettenleiter, M.; Neitzel, F. An intensity-based stochastic model for terrestrial laser scanners. *ISPRS J. Photogramm. Remote Sens.* **2017**, *125*, 146–155. [CrossRef]
19. Neuner, H.; Holst, C.; Kuhlmann, H. Overview on current modelling strategies of point clouds for deformation analysis. *Allgemeine Vermessungs-Nachrichten* **2016**, *123*, 328–339.
20. Ozendi, M.; Akca, D.; Topan, H. A generic point error model for TLS derived point clouds. In Proceedings of the Videometrics, Range Imaging, and Applications XIV, SPIE Optical Metrology, Munich, Germany, 25–29 June 2017. Proc. SPIE 10332, 103320J. [CrossRef]
21. Ozendi, M.; Akca, D.; Topan, H. Stochastic surface mesh reconstruction. In *The International Archives of the Photogrammetry, Remote Sensing and Spatial Information Sciences, Proceedings of the ISPRS TC II Mid-Term Symposium, Riva del Garda, Italy, 4–7 June 2018*; Volume XLII-2, pp. 805–812. Available online: https://www.int-arch-photogramm-remote-sens-spatial-inf-sci.net/XLII-2/805/2018/ (accessed on 1 November 2019). [CrossRef]
22. Stenz, U.; Hartmann, J.; Paffenholz, J.-A.; Neumann, I. A Framework Based on Reference Data with Superordinate Accuracy for the Quality Analysis of Terrestrial Laser Scanning-Based Multi-Sensor-Systems. *Sensors* **2017**, *17*, 1886. [CrossRef] [PubMed]
23. Wanner, M.C. *Verbundprojekt "Optimierung und Beurteilung des Oberflächenfinishs im Schiffbau (OFIN)", Teilprojekt "Entwicklung von Verfahren zur Beurteilung der Geometrischen Oberflächenqualität im Yachtbau". Schlussbericht, Berichtszeitraum: 01.07.2009 bis 30.06.2010*, 2010; unpublished.
24. Hexagon Metrology. Leica Absolute Tracker AT960 (Product Brochure). *Absolute Portability. Absolute Speed. Absolute Accuracy.* Available online: http://www.leica-geosystems.at/downloads123/m1/metrology/general/brochures/Leica%20AT960%20brochure_en.pdf (accessed on 26 November 2018).
25. Luhmann, T.; Müller, C. *Photogrammetrie Laserscanning Optische 3D-Messtechnik. Beiträge der Oldenburger 3D-Tage 2015*; Müller, L., Ed.; VDE Verlag: Heidelberg, Germany, 2015.
26. Walser, B.; Gordon, B. Der Laserscanner, eine Black-Box? In *Terrestrisches Laserscanning 2012 (TLS 2012), Proceedings of the 121. DVW-Seminar, Fulda, Germany, 13–14 Dezember 2012*; DVW—Gesellschaft für Geodäsie, Geoinformatik und Landmanagement e.V.: Augsburg, Germany, 2013.

27. Gielsdorf, F. Neue Wege bei der Registrierung von Scans. In *Terrestrisches Laserscanning 2013 (TLS 2013). Beiträge zum 132. DVW-Seminar, Fulda, Germany, 12–13 Dezember 2013*; DVW—Gesellschaft für Geodäsie, Geoinformatik und Landmanagement e.V.: Augsburg, Germany, 2013.
28. Paffenholz, J.-A.; Bae, K.-H. Geo-referencing point clouds with transformational and positional uncertainties. *J. Appl. Geod.* **2012**, *6*, 33–46. [CrossRef]
29. Gruen, A.; Akca, D. Least Squares 3D Surface and Curve Matching. *ISPRS J. Photogramm. Remote Sens.* **2005**, *59*, 151–174. [CrossRef]
30. Ehm, M.; Hesse, C. Entwicklung eines kinematischen Laserscansystems für Anwendungen im Schiffbau. In *Go-3D 2012 Computergraphik für die Praxis*; Fraunhofer IGD, Institutsteil Rostock: Hrsg, Rostock, 2012.
31. Hartmann, J.; Trusheim, P.; Alkhatib, H.; Paffenholz, J.-A.; Diener, D.; Neumann, I. High Accurate Pointwise (Geo-) Referencing of a K-TLS Based Multi-Sensor-System. *ISPRS Ann. Photogramm. Remote Sens. Spat. Inf. Sci. IV-4 (2018)* **2018**, *4*, 81–88. [CrossRef]
32. Lague, D.; Brodu, N.; Leroux, J. Accurate 3D comparison of complex topography with terrestrial laser scanner. Application to the Rangitikei canyon (N-Z). *ISPRS J. Photogramm. Remote Sens.* **2013**, *82*, 10–26. [CrossRef]
33. Strübing, T.; Neumann, I. Positions- und Orientierungsschätzung von LIDAR-Sensoren auf Multisensorplattformen. *Zeitschrift für Vermessungswesen* **2013**, *3*, 210–221.
34. Dorndorf, A.; Hartmann, J.; Paffenholz, J.-A.; Neumann, I.; Hesse, C. Validierung und Kalibrierung eines TLS-basierten Multi-Sensor-Systems. In *2015 Photogrammetrie Laserscanning Optische 3D-Messtechnik, Proceedings of the Beiträge der Oldenburger 3D-Tage 2015, Oldenburg, Germany, 4–5 February 2015*; Luhmann, T., Müller, C., Müller, L., Eds.; Vde Verlag GmbH: Heidelberg, Germany, 2015.
35. Heinz, E.; Eling, C.; Wieland, M.; Klingbeil, L.; Kuhlmann, H. Analysis of Different Reference Plane Setups for the Calibration of a Mobile Laser Scanning System. In Proceedings of the Ingenieurvermessung 17, Beiträge zum 18. Internationalen Ingenieurvermessungskurs, Graz, Austria, 25–29 April 2017. Lienhart, W., Hrsg.
36. Hartmann, J.; Paffenholz, J.-A.; Strübing, T.; Neumann, I. Determination of Position and Orientation of LiDAR Sensors on Multisensor Platforms. *J. Surv. Eng.* **2017**, *143*, 04017012. [CrossRef]
37. Mettenleiter, M.; Härtl, F.; Kresser, S.; Fröhlich, C. *Laserscanning—Phasenbasierte Lasermesstechnik für Die Hochpräzise und Schnelle Dreidimensionale Umgebungserfassung*; Verlag Moderne Industrie: München, Germany, 2015.
38. Timmen, A. Definition und Ableitung eines Qualitätsindexes zur Visualisierung der Qualitätsparameter von 3D-Punktwolken in einer Virtuellen Umgebung. Master's Thesis, Leibniz Universität Hannover, Hannover, Germany, 2016.
39. Hexagon Metrology. *Leica T-Scan 5 Brochure 2014*; Hartwig, Inc.: St. Louis, MO, USA, 2014.
40. Calkins, J. Quantifying Coordinate Uncertainty Fields in Coupled Spatial Measurement Systems. Ph.D. Thesis, Virginia Polytechnic Institute and State University, Montgomery, VA, USA, 2002.
41. JCGM. *Evaluation of Measurement Data—Guide to the Expression of Uncertainty in Measurement (GUM 1995 with Minor Corrections, ISO/IEC Guide 98-3)*; International Organization for Standardization: London, UK, 2008.
42. Balch, M. *Complete Digital Design: A Comprehensive Guide to Digital Electronics and Computer System Architecture*; McGraw-Hill Education: New York, NY, USA, 2003.
43. Müller-Stoy, P. Zukünftige Rechnerarchitekturen. In *Die Zukunft der Informationssysteme Lehren der 80er Jahre, Proceedings of the Dritte gemeinsame Fachtagung der Österreichischen Gesellschaft für Informatik (ÖGI) und der Gesellschaft für Informatik (GI) Johannes Kepler Universität Linz, Linz, Austria, 16–18 September 1986*; Schulz, A., Ed.; Springer: Berlin/Heidelberg, Germany, 1986.
44. Hennes, M. Zur raumzeitlichen Datenerfassung. In Proceedings of the Zeitabhängige Messgrößen—Ihre Daten haben (Mehr-)Wert, 129. DVW-Seminar, Hannover, Germany, 26–27 February 2014.